Strain hardening effect on ductile tearing under small scale yielding plane strain conditions

Antonio Kaniadakis[a], Van-Dung Nguyen[a,b], Jacques Besson[c], Thomas Pardoen[a,d,]

[a] *Institute of Mechanics, Materials and Civil Engineering, UCLouvain, Place Sainte Barbe 2, Louvain la Neuve, B-1348, Belgium*
[b] *Computational & Multiscale Mechanics of Materials, Department of Aerospace and Mechanical Engineering, University of Liège, Allée de la découverte 9, Liège, B-4000, Belgium*
[c] *Mines Paris, PSL Research University, Centre des Matériaux, CNRS UMR 7633, 63–65 rue Henri-Auguste Desbruères, Corbeil-Essonnes, 91003, France*
[d] *WEL Research Institute, Avenue Pasteur 6, Wavre, B-1300, Belgium*

Abstract

The effect of strain-hardening on ductile crack growth is explored based on a small scale yielding finite element approach using an advanced nonlocal Gurson model. A focus is put on considering high strain hardening exponent n up to 0.5, while classical literature is often limited to $n = 0.2$, in order to encompass materials like stainless steels as well as several modern TRIP-TWIP alloys and high entropy alloys. First, J_2 plasticity-based simulations are performed to set the static crack reference. These simulations provide a hint about the origin of the increase of fracture toughness with increasing n, connected to much smaller finite strain zones at a given loading level quantified by the value of the J integral. In addition, it is found that above $n \sim 0.3$, the opening stress does not attain a maximum value at a distance equal to one to two crack openings but keeps increasing towards the surface of the blunted crack tip. Then, Gurson-based simulations are used to determine the J_R curve for different n and initial porosity, and associated quantities related to crack initiation such as J_{Ic}, critical crack tip opening displacement δ_c, and fracture process zone length. As already found in earlier studies, both J_{Ic} and δ_c increase with increasing n, although the effect is much more marked on J_{Ic}. The origin of this first-order effect is unraveled by looking at the stress triaxiality, damage, and plastic strain fields. Even though the near crack tip stress triaxiality increases with n, the associated lower plastic strain at a fixed distance to the crack front leads to much lower void growth rates and delays void coalescence. As a important side result, the simulations appear very sensitive to an accurate fine-tuning of the adjustment factors entering the Gurson model at high strain hardening, pointing towards the intrinsic limitations of the model when n is large. This study confirms the interest in developing alloys with large strain hardening capacity, not only with respect to tensile properties but also in view of enhancing the ductile fracture toughness.

Keywords: Strain hardening, Ductile Failure, Fracture toughness, J-integral

1. Introduction

Novel metallic alloys with superior mechanical performance have been developed over the last two decades, often by increasing the strain hardening capacity. This is reflected by strain hardening exponents, when expressed in terms of power law hardening, well above 0.2, typically up to 0.5 and sometimes higher. These new or optimized classes of alloys include, among others, TWIP steels (De Cooman et al., 2018), TRIP steels (Grässel et al., 2000), novel Ti alloys (Schaal et al., 2023), (Eleti et al., 2020), and high entropy alloys (Hilhorst et al., 2023). Now, some traditional alloys also exhibit very large strain hardening capacity such as stainless steels, brass, certain aluminum alloys, and nickel-based superalloys. The advantages of a large strain hardening exponent are numerous: (i) formability is improved through higher resistance to plastic localization (Yoshida and Kuwabara, 2007), (ii) very large strength can be attained by cold forming through accumulating large plastic strains while keeping sufficient uniform elongation, and, (iii) even

Email address: thomas.pardoen@uclouvain.be (Thomas Pardoen)

though it is still less appreciated, a higher fracture toughness, see Pardoen and Hutchinson (2003). This last effect sets the motivation of the present study.

Several micromechanics-based studies of ductile crack growth relying on a description of the damage process with a Gurson-type model, as schematically sketched in Fig. 1, indicated that fracture toughness of metallic alloys increases with increasing strain hardening capacity (see Xia et al. (1995), Pardoen and Hutchinson (2003) and Pardoen et al. (2004)). This is considering that all other relevant parameters are kept constant, e.g., initial yield stress, elastic modulus, initial void volume fraction, and population of inclusion responsible for extra void nucleation, temperature. However, the reason for the fracture toughness increase has not been fully unraveled based on quantitative reasoning. Clearly, it is not because the true fracture strain ε_f as measured in uniaxial tension increases with strain hardening that the fracture toughness increases; the reason for this increase of ε_f in uniaxial tensile tests is related to late necking and postponed elevation of the stress triaxiality in the neck, an argument that does not apply to a fracture process zone (FPZ) at least under plane strain or near-plane strain conditions.

The typical variation of the opening stress, stress triaxiality, and equivalent plastic strain as a function of the normalized distance to the crack tip is reminded in Fig. 1 for a static crack in an elastoplastic solid. The finite strain zone extends over a distance of 1 to 2 crack tip opening displacements. This is also the distance needed to build up the high stress triaxiality levels from 3 to 5, and associated peak opening stress equals 3 to 5 times the yield stress. Remember that the stress triaxiality at the blunted crack tip is precisely equal to the plane strain tension value of 0.577. This is the picture that emerged from the seminal large strain elastoplastic studies of static cracks starting from slip line analysis by Rice and Johnson (1969) followed by finite element (FE) simulation by McMeeking (1977) for static cracks. As a matter of fact, almost all these studies limited themselves to power law hardening representation with strain hardening exponent up to 0.2. These analyses were extended by Rice and Sorensen (1978) and Hutchinson (1974) for growing cracks. The reason for focusing on $n \leq 0.2$ was most probably that this is a sort of upper value for most traditional structural aluminum alloys and ferritic steels. This justifies in the first part of this paper a preliminary reassessment of the J_2 elastoplastic analysis of static cracks at high n to verify if the picture of Fig. 1 is still valid.

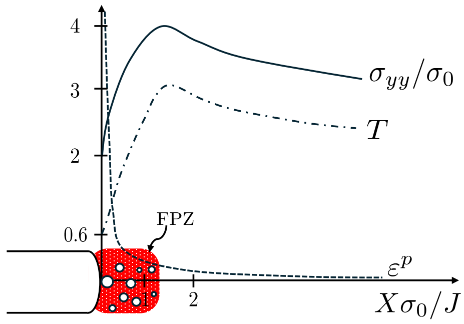

Figure 1: Qualitative illustration of the fracture process zone, of the evolution of the opening stress σ_{yy}/σ_0, stress triaxiality T, and accumulated plastic strain ε^p as a function of the normalized distance to the crack tip.

More advanced analysis of ductile tearing appeared later in the frame of FE simulations with discrete voids, e.g. Aravas and McMeeking (1985), Hutchinson and Tvergaard (1989), Narasimhan and Rosakis (1988); with cohesive zone based models based (Tvergaard and Hutchinson, 1992); or with damage based simulations, see e.g. Xia and Shih (1995), O'Dowd et al. (1995), Gullerud et al. (1999), and Pardoen and Hutchinson (2000). The last class of simulations is the most versatile in terms of the richness of the description of the damage process put in the model while not being subjected to the limitations of the cohesive zone model which can only be connected indirectly to the micromechanics of ductile fracture, e.g., Tvergaard and Hutchinson (1992). One of the difficulties with Gurson-based simulations (or with any other damage models) is the absence of length scale and intrinsic mesh dependency. Hence, nonlocal versions have been developed, see Zhang et al. (2018), Chen et al. (2020), Nguyen et al. (2020), Espeseth et al. (2023). Again, the focus has essentially been put in all these works on small to moderate strain hardening capacity with n typically not larger than 0.2.

The goal of this work is to investigate the effect of strain hardening on the ductile tearing resistance, first by setting J_2 plasticity references for a static crack and then using an advanced Gurson model to simulate crack initiation and growth, with a specific focus on high values of n up to 0.5, a value typical for stainless steel. The questions are: (i) why is J_{Ic} fundamentally increasing with n? (ii) how does very large n affect fracture resistance indicators? (iii) what is the impact of future metallic alloys development with high strain hardening capacity? In order to avoid entering complex discussions regarding constraint effects associated with finite cracked test geometries, a small scale yielding (SSY) formalism is invoked. It consists of simulating a vast material domain, including a long crack, by imposing the K-field solution at the periphery. Several rules are followed to guarantee that small scale yielding conditions are ensured, but also that the results are not dependent on the choice of the initial crack tip opening and nonlocal length. Care will be taken to fine-tune the parameters of the advanced Gurson model to predict void growth rates and coalescence in agreement with void cell simulations performed for the different initial porosities and strain hardening exponents. The key results extracted from the SSY simulations are the stress, plastic strain and damage parameters fields, FPZ length, J_R curve, tearing modulus, crack tip opening, and J values as well as their values at cracking initiation δ_c and J_{Ic}, and the tearing modulus T_J.

The paper starts by presenting the constitutive equations and SSY formalism. The results of the J_2 simulations and Gurson simulations, after calibration of the Gurson and Thomason parameters, are presented in the following section. The discussion in Section 4 aims at elucidating the root cause of the positive effect of the strain hardening on fracture toughness while also addressing the comparison with other results available in the literature and the ultra-high opening stress.

2. Constitutive models and SSY formalism

The hardening law is presented before introducing the two constitutive models: the classical J_2 flow theory and the advanced nonlocal Gurson model. The principles of the SSY model are explained next, with the geometric configuration and the plane strain condition, the meshing strategy, and the methodology for computing the crack length.

2.1. Hardening law

A Swift hardening law is considered to describe the strain hardening of the material as expressed by:

$$\sigma_Y = \sigma_0 \left(1 + k\varepsilon^p\right)^n , \tag{1}$$

where σ_Y is the current yield, σ_0 is the initial yield stress, n is the strain hardening exponent, ε^p is the accumulated plastic strain, and k is a hardening parameter. The ratio σ_0/E (with E the Young's modulus) is kept equal to 666. Fig. 2 plots the hardening laws for different values of the strain hardening exponent and k parameter addressed in this work. The goal is mainly to insist on the huge level of strength that is attained with $n = 0.5$ possibly going above $10\sigma_0$ at $\varepsilon^p = 1$ depending on the value of k. An equivalent plastic strain of 1 is not unrealistic for very tough ductile metals in the near crack tip zone, as it will be shown later.

2.2. Constitutive models

2.2.1. J_2 elastoplasticity

Isotropic linear elasticity is described by Hooke's law with Young's modulus E and Poisson ratio ν always taken equal to 0.3. The J_2 yield locus writes

$$\Phi_{J_2} = \frac{\sigma_{eq}}{\sigma_Y} - 1 = 0, \tag{2}$$

with $\sigma_{eq} = \sqrt{\frac{3}{2}\mathrm{dev}(\boldsymbol{\sigma}) : \mathrm{dev}(\boldsymbol{\sigma})}$ the equivalent von Mises stress, $\boldsymbol{\sigma}$ the corotational Cauchy stress tensor, whereas the plastic normal to the yield surface is obtained as

$$\mathbf{N}^p = \mathbf{N}^p_{J_2} = \sigma_Y \frac{\partial \Phi_{J_2}}{\partial \boldsymbol{\sigma}} = \frac{\partial \sigma_{eq}}{\partial \boldsymbol{\sigma}} . \tag{3}$$

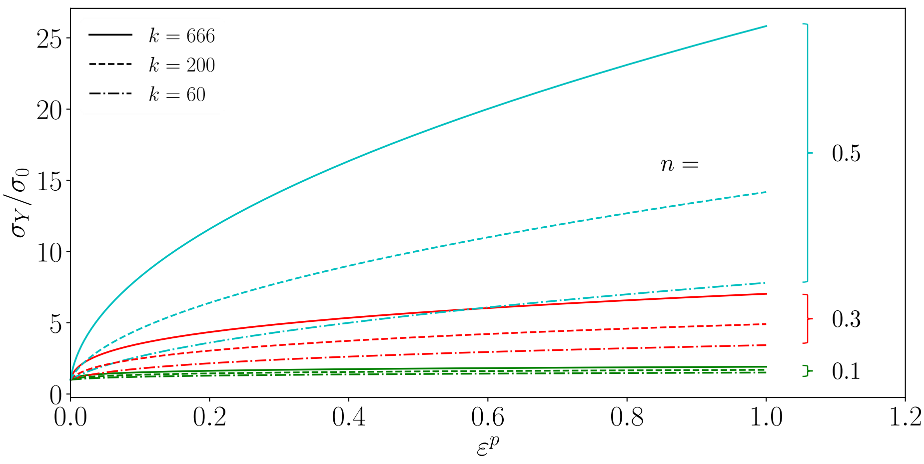

Figure 2: Hardening law for different strain hardening exponents and values of k.

2.2.2. *Advanced nonlocal Gurson model*

The version of the Gurson model extended by Nguyen et al. (2020) includes three distinct solutions for describing the ductile damage process: void growth, void coalescence by internal necking, and shear-driven void coalescence. These three solutions are each cast in the form of a yield locus. These three yield loci are then assembled into one for the sake of optimizing the numerical implementation and avoiding the difficulties associated to transitioning from one solution to another. Since the analysis considers void coalescence by internal necking only, shear-driven coalescence is not presented hereafter. The model aims at representing the behavior of a solid including a distribution of voids that can be described based on a representative cylindrical unit cell with a void at the center as depicted in Fig. 3. The choice of referring to a cylindrical cell that remains cylindrical is an approximation of the plane strain problem addressed in this study. We will discuss this point later. The dimensionless variables that characterize the unit cell

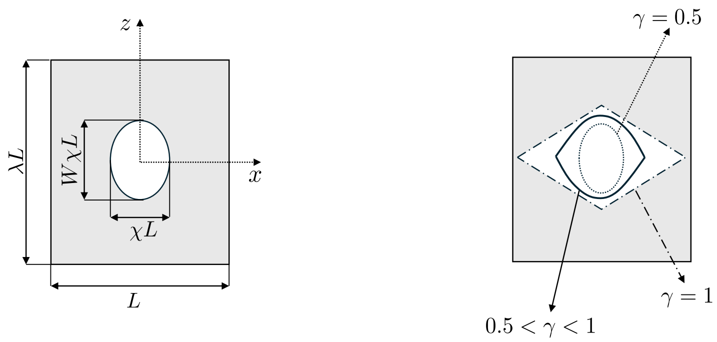

Figure 3: Cylindrical unit cell with a void and associated geometrical parameters.

are the porosity f, the void aspect ratio W, the void ligament ratio χ, the void spacing ratio λ, and the main axis z of the void with unit vector $\mathbf{e}_z$. During the void growth phase, W is equal to 1 as the GTN model considers spherical voids. The parameter γ describes the shape of the void, which, during coalescence, will be altered owing to specific geometry evolution laws (see Fig. 3). For a spheroidal void $\gamma = \frac{1}{2}$, while $\gamma = 1$ for a cone. The parameters are related via

$$f = \frac{\chi^3 W}{3\gamma\lambda}. \tag{4}$$

Following Nguyen et al. (2020), the vector describing the void characteristics is

$$\mathbf{Y} = \begin{bmatrix} f & \chi & W & \lambda & \gamma & \mathbf{e}_z \end{bmatrix}^T, \tag{5}$$

with

$$\mathbf{Y}_0 = \begin{bmatrix} f_0 & \chi_0 & W_0 & \lambda_0 & \gamma_0 & \mathbf{E}_z \end{bmatrix}^T, \tag{6}$$

the vector with the initial values. The porous plasticity model is characterized by the following equations:

$$\Phi_{nl} = \Phi_{nl}\left(\boldsymbol{\sigma}; \sigma_Y, \mathbf{Y}\right), \tag{7}$$

$$\mathbf{D}^p = \dot{\mu}\mathbf{N}^p\left(\boldsymbol{\sigma}; \sigma_Y, \mathbf{Y}\right), \tag{8}$$

$$\boldsymbol{\sigma} : \mathbf{D}^p = (1 - f)\,\sigma_Y \dot{\varepsilon}_m, \tag{9}$$

$$\dot{\mathbf{Y}} = \dot{\mathbf{Y}}\left(\mathbf{Y}, \bar{\mathbf{Z}}, \boldsymbol{\sigma}\right), \tag{10}$$

$$\dot{\mu} \geq 0, \Phi_{nl} \leq 0, \dot{\mu}\Phi_{nl} = 0, \tag{11}$$

where Φ_{nl} is the yield function, σ_Y the mean yield stress of the matrix that follows Eq. (1), $\mathbf{D}^p$ the plastic strain rate, with plastic normal $\mathbf{N}^p$, ε_m the matrix equivalent plastic strain, μ the plastic multiplier, and $\bar{\mathbf{Z}}$ a vector including all nonlocal variables. The deviatoric and volumetric equivalent plastic strain rates read respectively

$$\dot{\varepsilon}_d = \sqrt{\frac{2}{3}\mathrm{dev}\left(\mathbf{D}^p\right) : \mathrm{dev}\left(\mathbf{D}^p\right)}, \qquad \dot{\varepsilon}_v = \mathrm{tr}\left(\mathbf{D}^p\right). \tag{12}$$

Like in Nguyen et al. (2020), the matrix, deviatoric, and volumetric equivalent plastic strains are selected as local variables and indicated by $\mathbf{Z}$, with their nonlocal counterparts being $\bar{\mathbf{Z}}$ as

$$\mathbf{Z} = \begin{bmatrix} \varepsilon_v & \varepsilon_m & \varepsilon_d \end{bmatrix}^T, \qquad \bar{\mathbf{Z}} = \begin{bmatrix} \bar{\varepsilon}_v & \bar{\varepsilon}_m & \bar{\varepsilon}_d \end{bmatrix}^T. \tag{13}$$

The relationship between the local and nonlocal variables following the implicit nonlocal model (Peerlings et al., 1998) is given by

$$\bar{Z}_k - Z_k - \nabla_0 \cdot \left(\mathbf{C}_k \cdot \nabla_0 \bar{Z}_k\right) = 0, \tag{14}$$

where $k = 1, \ldots, N$ denotes the possible nonlocal mechanisms. $\mathbf{C}_k = l_k^2\mathbf{I}$ represents the second order nonlocal length tensor, with l_k the nonlocal length associated with the nonlocal mechanism k. Here, we will assume only one mechanism associated with one nonlocal length noted l_{nl}.

Void growth phase: GTN model. Void growth is modeled by the Gurson-Tvergaard-Needleman GTN model (Needleman and Tvergaard (1984); Tvergaard and Needleman (1984)). Eq. (7) is rewritten using the GTN yield function

$$\Phi_{nl} = \Phi_G = \frac{\hat{\sigma}_G}{\sigma_Y} - 1, \tag{15}$$

with $\hat{\sigma}_G$ the GTN effective stress, defined as

$$\hat{\sigma}_G\left(\sigma_{eq}, p', \sigma_Y, f\right) = \frac{\sqrt{\sigma_{eq}^2 + 2\sigma_Y^2 f q_1 \left[\cosh\left(\frac{3}{2}q_2\frac{p'}{\sigma_Y}\right) - 1\right]}}{1 - q_1 f}, \tag{16}$$

where $\sigma_{eq} = \sqrt{\frac{3}{2}\mathrm{dev}(\boldsymbol{\sigma}) : \mathrm{dev}(\boldsymbol{\sigma})}$ is the equivalent von Mises stress, $p' = \frac{\mathrm{tr}(\boldsymbol{\sigma})}{3}$ is the hydrostatic stress, and q_1 and q_2 are the fitting constants introduced by Tvergaard (1981). The plastic normal to the GTN yield surface writes

$$\mathbf{N}^p = \mathbf{N}_G^p = \sigma_Y\frac{\partial\Phi_G}{\partial\boldsymbol{\sigma}} = \frac{\partial\hat{\sigma}_G}{\partial\boldsymbol{\sigma}}. \tag{17}$$

Regarding the evolution laws of the void characteristics, as mentioned above, the voids are initially spherical, i.e., $W_0 = 1$ and $\gamma_0 = 0.5$ and preserve their shape during void growth ($\dot{W} = 0$, $\dot{\gamma} = 0$). The evolution laws of $\mathbf{Y}$ read

$$\begin{cases} \dot{f} = (1-f)\dot{\bar{\varepsilon}}_v + A_n(\bar{\varepsilon}_m)\dot{\bar{\varepsilon}}_m \\ \dot{W} = 0 \\ \dot{\lambda} = \kappa\lambda\dot{\bar{\varepsilon}}_d \end{cases}, \tag{18}$$

where two terms contribute to the porosity evolution: the void growth term $(1-f)\dot{\bar{\varepsilon}}_v$ and the nucleation term $A_n(\varepsilon_m)\dot{\bar{\varepsilon}}_m$, see Chu and Needleman (1980). A_n represents the nucleation intensity function

$$A_n = \frac{f_N}{s_N\sqrt{2\pi}}\exp\left(-\frac{1}{2}\left(\frac{\varepsilon_m - \varepsilon_N}{s_N}\right)^2\right) \tag{19}$$

with f_N the volume fraction of inclusions at which damage can be nucleated, ε_N the strain at which half of the inclusions have generated a void, s_N the standard deviation on the nucleation strain. The parameter κ is the void distribution factor, see Benzerga et al. (2016).

The evolution of the ligament ratio χ is given by

$$\chi = \left(\frac{3f\lambda}{2}\right)^{\frac{1}{3}}. \tag{20}$$

Internal-necking void coalescence: MPS-based Thomason yield function. The yield surface describing the response of the porous solid during the internal necking stage writes

$$\Phi_{nl} = \Phi_T = \frac{\hat{\sigma}_T}{\sigma_Y} - 1, \tag{21}$$

where Φ_T is the Thomason yield surface, with $\hat{\sigma}_T$ the associated effective stress

$$\hat{\sigma}_T = \frac{1}{C_{Tf}}\left(\frac{2}{3}\sigma_{eq}\cos\theta + |p'|\right). \tag{22}$$

In Eq. (22), C_{Tf} represents the plastic constraint factor, see Pardoen and Hutchinson (2003), given by

$$C_{Tf} = \frac{3}{2}\left(1-\chi^2\right)\left[\alpha\left(\frac{1-\chi}{\chi W}\right)^2 + \beta\sqrt{\frac{1}{\chi}}\right], \tag{23}$$

where α and β are constants, which can depend on the strain hardening exponent (Pardoen and Hutchinson, 2000), and θ is the Lode angle given by $\theta(\sigma_{eq}, J_3) = \frac{1}{3}\arccos\frac{27J_3}{2\sigma_{eq}^2}$, with $J_3 = \det(\mathrm{dev}(\boldsymbol{\sigma}))$. The plastic normal now reads

$$\mathbf{N}^p = \mathbf{N}_T^p = \sigma_Y\frac{\partial\Phi_T}{\partial\boldsymbol{\sigma}} = \frac{\partial\hat{\sigma}_T}{\partial\boldsymbol{\sigma}}, \tag{24}$$

whereas the evolution laws for the geometry are expressed by

$$\begin{cases} \dot{\chi} = \dfrac{3}{4}\dfrac{\lambda}{W}\left(\dfrac{3}{2\chi^2} - 1\right)\dot{\bar{\varepsilon}}_d \\ \dot{W} = \dfrac{9}{4}\dfrac{\lambda}{\chi}\left(1 - \dfrac{1}{2\chi^2}\right)\dot{\bar{\varepsilon}}_d \\ \dot{\lambda} = \kappa\lambda\dot{\bar{\varepsilon}}_d \end{cases} . \tag{25}$$

Effective yield surface. The effective yield surface Φ_e combining Φ_G and Φ_T is introduced

$$\Phi_{nl} = \Phi_e = \max\left(\Phi_G, \Phi_T\right). \tag{26}$$

Thus, the space of admissible solutions is delimited by the two yield surfaces Φ_G and Φ_T. Eq. (26) can be rewritten as

$$\Phi_e = \frac{\hat{\sigma}}{\sigma_Y} - 1, \tag{27}$$

with

$$\hat{\sigma} = \max\left(\hat{\sigma}_G, \hat{\sigma}_T\right), \tag{28}$$

Void coalescence is assumed to start when $\dot{\varepsilon}_m > 0$ and

$$\hat{\sigma}_T > \hat{\sigma}_G. \tag{29}$$

This model has been validated by comparison to experimental data on high entropy alloys in Hilhorst et al. (2022).

2.3. SSY model

2.3.1. Model description and quantities of interest

Fig. 4 describes the SSY model. It assumes a circular region of external radius R_{ext} with a notch of initial opening δ_0. Displacement-controlled boundary conditions are applied on the outer boundary. The two components of the displacement $\mathbf{u}$ along the x and y direction read for mode I

$$u_x(r,\theta) = \frac{K_I\left(1+\nu\right)}{E}\sqrt{\frac{r}{2\pi}}\cos\frac{\theta}{2}\left(3 - 4\nu - \cos\theta\right), \tag{30}$$

$$u_y(r,\theta) = \frac{K_I\left(1+\nu\right)}{E}\sqrt{\frac{r}{2\pi}}\sin\frac{\theta}{2}\left(3 - 4\nu - \cos\theta\right), \tag{31}$$

with K_I the stress intensity factor, ν the Poisson ratio, and (r,θ) the polar coordinates, see Fig. 4. The J integral is related to the stress intensity factor K_I by

$$J = \frac{K_I^2\left(1-\nu^2\right)}{E}. \tag{32}$$

The radius of the plastic zone R_p under plane strain conditions is approximated by

$$R_p = \frac{1}{3\pi}\left(\frac{K_I}{\sigma_0}\right)^2, \tag{33}$$

although the exact values can obviously be extracted from the SSY simulations.

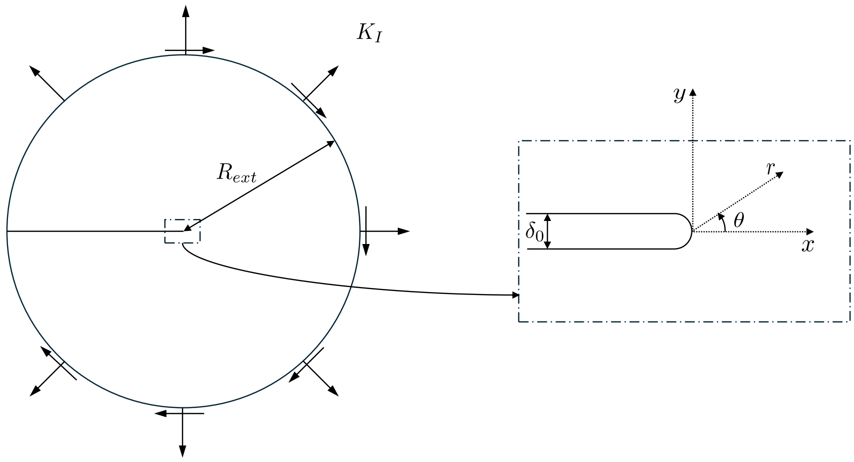

Figure 4: Illustration of the SSY geometry with zoom on the initial crack tip and polar coordinates system.

2.3.2. *Validity conditions for SSY model*

Several conditions must be verified to ensure the simulations give meaningful results and respect the SSY condition.

1. The external radius R_{ext} must be considerably larger than the size of the plastic zone R_p during cracking, which, as shown by Eq. (33), depends on the applied loading. Chen et al. (2020) suggested $R_p \leq 0.05R_{ext}$. As an alternative, to verify the SSY assumption, three different domains are defined to compute the J integral and compare it to the theoretical value of Eq. (32). The domains can be visualized in Fig. 5a). Each domain is delimited by an internal radius R_{int} and an outer radius R_{out}. The first domain (blue surface of Fig. 5a)) has $R_{out} = R_{ext}$ and $R_{int} \approx 0.02R_{ext}$. The second domain (orange surface) is characterized by $R_{out} \approx 0.02R_{ext}$ and $R_{int} \approx 0.01R_{ext}$, and the third domain (green surface) has $R_{out} \approx 0.01R_{ext}$ and $R_{int} \approx 0.003R_{ext}$. Fig. 5b) portrays the comparison of the value of the J integral computed on the three domains of Fig. 5a) (J^{Domain}) with the theoretical J given by $K_I^2(1-\nu^2)/E$ for different strain hardening exponents using the GTN model. Discussion of these results will come later in the paper. J^{Domain} matches perfectly J until a certain level of applied loading. After that, the outer domain gives a value much closer to the expected applied J as it does not encompass the region with very high plastic deformation, crack propagation and thus non-radial loading. For this study, it is checked that at the onset of cracking $J^{Domain} \approx J$ to within 1%.
2. The initial crack tip opening δ_0 must be chosen to be smaller than the critical crack tip opening displacement δ_c. This condition can only be verified a posteriori or by running simulations with different δ_0. The sensitivity analysis on δ_0 is addressed in Appendix C.
3. The initial crack tip opening δ_0 must be smaller than the nonlocal length l_{nl}. The nonlocal length is, in principle, related in one way or another to a physical length scale if the model is consistent and physically realistic. More precisely, in ductile fracture, it should be commensurate with the void spacing. Hence, this nonlocal length should set a physical dimension related to the microstructure. A starter crack can be considered a sharp crack if its opening is smaller than the microstructure length driving the failure process; otherwise, it acts more as a notch with respect to the length scale over which the gradient of stress and strain must encompass the damage mechanisms.

Other conditions related to the mesh refinement are described next.

2.3.3. *Meshing*

Fig. 6 presents a typical mesh. In the far region, which deforms elastically, a coarser mesh can be used, whereas near the original crack tip and along the crack path, a very fine mesh is required as set also by the nonlocal length l_{nl}. Initially $\delta_0 = l_{nl}$ and $R_{ext} = 55000l_{nl}$ are set. Systematic mesh refinement studies have been performed to set the magnitude of the element size l_e as a function of l_{nl} that leads to results independent of mesh density. Fig. 7 shows the J_R curves for the case $n = 0.5$ and $f_0 = 10^{-2}$ obtained with $l_e = 0.33l_{nl}$, $l_e = 0.20l_{nl}$, $l_e = 0.16l_{nl}$, and $l_e = 0.10l_{nl}$.

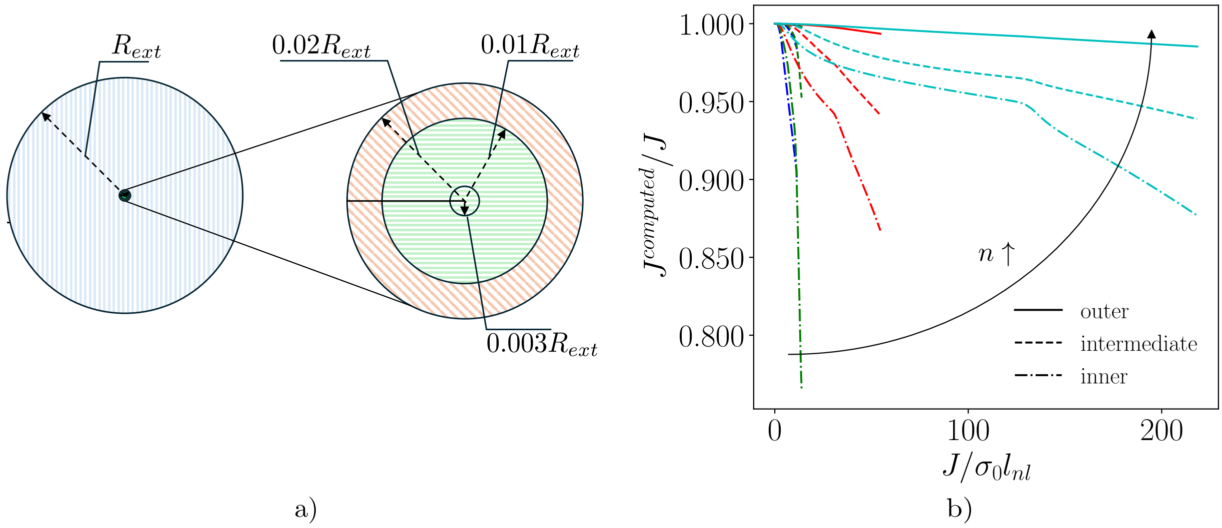

Figure 5: a) Illustration of the three domains used to compute the J integral: the outer domain (blue), the intermediate domain (orange), and the inner domain (green). b) Comparison between the theoretical value of J and the numerical value computed from the three domains for four values of the strain hardening exponent $n = 0.01$, $n = 0.1$, $n = 0.3$, and $n = 0.5$.

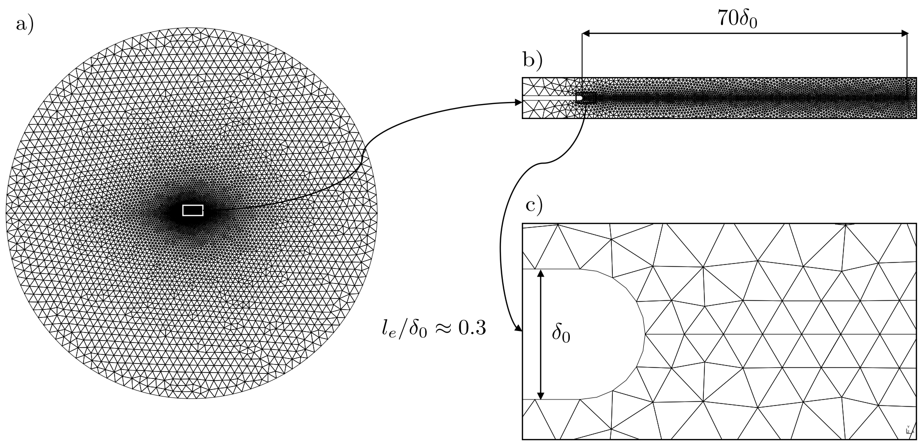

Figure 6: Finite element mesh of the SSY model with two levels of zooming: a) far from the crack tip; b) in the FPZ; c) around the crack tip.

The results are mesh independent; the mesh with $l_e = 0.33 l_{nl}$ is thus selected. In Chen et al. (2020) l_e was taken equal to $0.35 l_{nl}$, almost identical to here.

A more comprehensive mesh convergence study demonstrating that the results are mesh objective can be found in Appendix A.

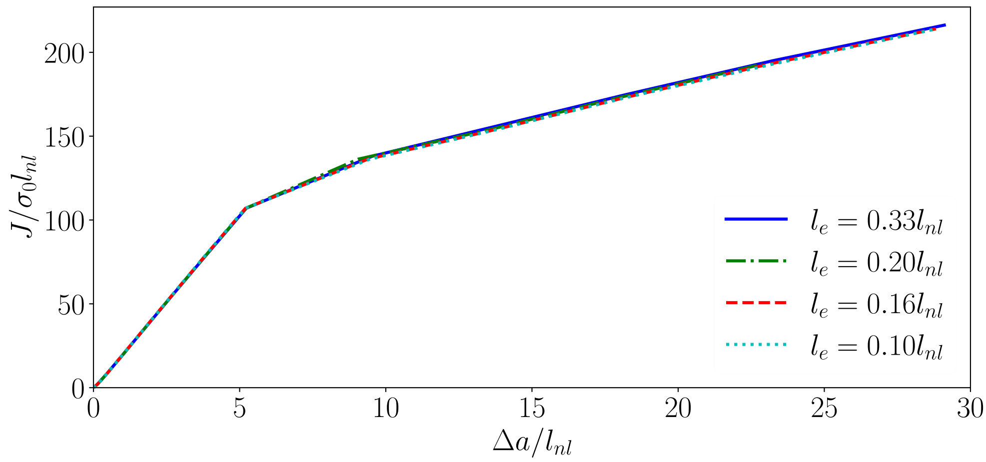

Figure 7: Result of the mesh objectivity analysis in terms of the J_R curve for four different mesh densities, with $n = 0.5$ and $f_0 = 10^{-2}$.

2.4. *Crack length definition*

Fig. 8 is a schematic to explain how the crack length Δa is extracted from the simulations. X_{ref} represents the position of the initial crack tip (at the extremity of the starter crack) in the initial *undeformed* configuration. With increasing applied loading, the crack opens, and the position in the *current* configuration becomes x_{ref}. This latter will be used to compute the crack length. Then, at a certain loading, the crack starts propagating, leading to an evolving crack front. The position x_{tip} is the furthest in the x direction that satisfies the failure condition. This failure condition is a function $f(x)$ that describes the onset of coalescence. As soon as this value reaches unity, cracking is considered to initiate. Note that experimentally, the crack advance Δa includes the pseudo propagation u associated with the blunting process, hence called Δa-blunting. The crack length is given by

$$\Delta a \equiv x_{tip} - x_{ref}, \tag{34}$$

where

$$x_{tip} = \max\left(x, f(x) = 1\right), \qquad x_{ref} = X_{ref} + u, \qquad f(x) = \text{"COALESCENCE"}. \tag{35}$$

3. Results of the parametric study with SSY framework

3.1. *J_2 elastoplastic simulations*

For the elastoplastic static crack case, the material is characterized by $k = 666$ and various strain hardening exponents n from 0.1 to 0.5.

Fig. 9 shows the variation of a) the opening stress and b) the stress triaxiality ratio T (T is defined as p'/σ_{eq}, i.e. the ratio of the hydrostatic stress to equivalent stress) as a function of the distance to the crack tip X defined in the initial configuration (and normalized by the product of initial yield stress and J), for different values of applied J. The elements close to the initial crack tip are subject to very high deformation and distortion; results when $\varepsilon^p \geq 1.5$ are not considered.

In the subsequent analysis, results will be shown for J values above which the maximum opening stress and stress triaxiality reach a steady profile when plotted as a function of $X\sigma_0/J$. This is the case when $J/\sigma_0\delta_0 \geq 14$, whereas for

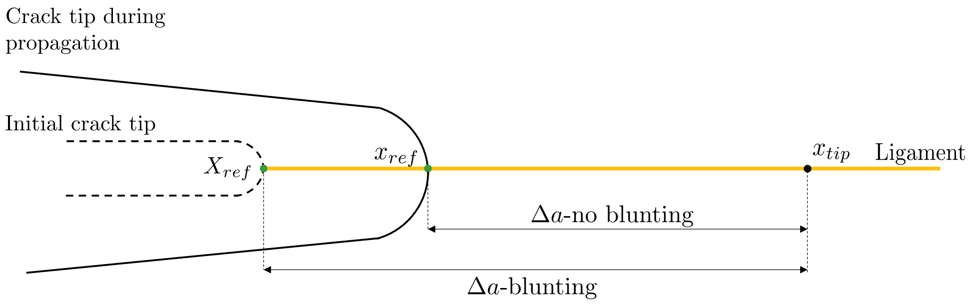

Figure 8: Definition of crack length with and without blunting.

$J/\sigma_0\delta_0 \leq 14$ there are not enough elements inside the FPZ (the FPZ is defined here as the region where $\varepsilon^p \geq 0.1$) to describe the material behavior accurately enough. This condition can also be written in terms of the crack tip opening displacement δ: since $J/\sigma_0 = \delta/d_n$, $J/\sigma_0\delta_0 \geq 14$ leads to

$$\delta \geq 14 d_n \delta_0, \tag{36}$$

with d_n the Shih factor (ranging typically between 0.1 at high n and 1 for low n). Eq. (36) appears to be fulfilled even for the higher values of the strain hardening exponent n as it can be seen in Fig. 9b). **In other words, J has to be large enough so that the initial notch effect is erased and the crack becomes a real crack in the sense of fracture mechanics. Another interpretation arising from Eq. (36) is that J has to be large enough so that a crack tip opening displacement much larger than δ_0 is attained**. This value depends on the strain hardening capacity through the Shih factor. This precaution is sometimes overlooked in the literature and is worth considering to produce reliable results.

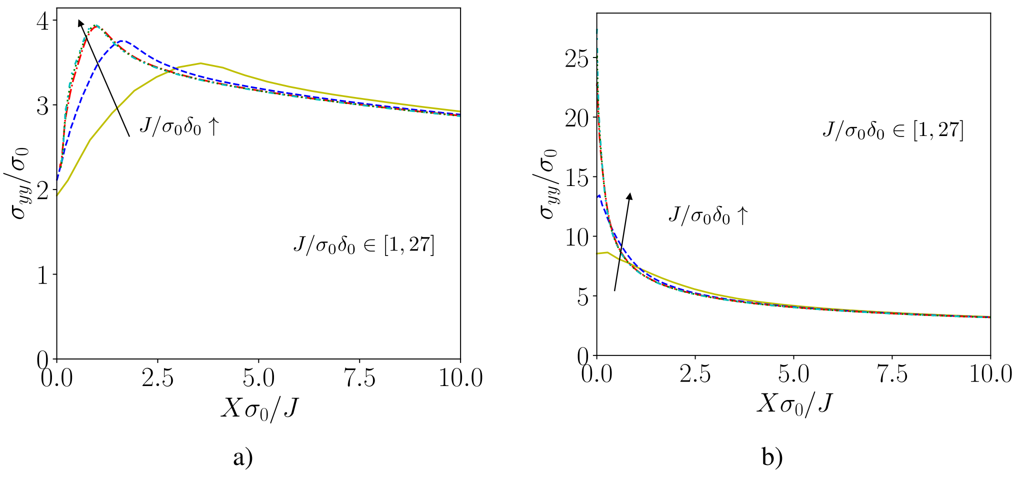

Figure 9: Opening stress evolution as a function of the normalized position for $n = 0.1$ a) and $n = 0.5$ b).

Figs. 10 and 11 reveal the influence of the strain hardening exponent on the opening stress σ_{yy} and on the accumulated plastic strain ε^p, on the stress triaxiality T, on the maximum stress triaxiality, on the fracture process zone FPZ size and on the crack tip opening displacement δ, here used to compute the Shih factor. Fig. 10a) illustrates that a low value of the strain hardening exponent n leads to lower maximum values of σ_{yy}/σ_0 in agreement with the HRR solution, see Rice and Rosengren (1968) and Hutchinson (1968). For higher values of n, the coordinate at which the maximum opening stress is reached shifts closer to the crack tip. A particularly unexpected result is that the traditional picture regarding the maximum opening stress that should be located at $X \approx 1$ to 2δ with values between 3 and $5\sigma_0$, is not true anymore for $n > 0.3$. The HRR solution for the opening stress for $n = 0.5$ is also represented in Fig. 10a). The stress field ahead of the crack tip reads

$$\frac{\sigma_{yy}(\theta=0)}{\sigma_0} = \left(\frac{J}{X\sigma_0}\frac{1}{\varepsilon_0 I_n}\right)^{\frac{n}{n+1}} \tilde{\sigma}_{\theta\theta}(\theta=0,n), \tag{37}$$

with $I_n = 5.94$ and $\tilde{\sigma}_{\theta\theta}(\theta = 0, n) = 1.6758$ for $n = 0.5$. The HRR solution and the numerical solution agree well for $0.1 < X\sigma_0/J < 0.5$. The difference increases for $X\sigma_0/J < 0.1$, with the peak stress of the HRR solution going to infinity, as the HRR analysis is based on a small strain formalism. Regarding the accumulated plastic strain, Fig. 10b) shows that materials with higher strain hardening capacity exhibit lower accumulated plastic strain for the same value of J. Moreover, the plastic deformations are concentrated closer to the crack tip for large values of n.

In order to consolidate these unconventional results, simulations have been repeated with the FE code Zebulon of the Z-set suite, see Besson and Foerch (1997), and are detailed in Appendix D, giving perfect agreement with the results of Fig. 9. This analysis has also been repeated for other values of k. The impact of this finding will be discussed in Section 4.

Fig. 10c) and 10d) show the variation of the stress triaxiality as a function of the normalized position. As expected, higher values of T are found when considering materials with high strain hardening capacity, showing a linear increase of T^{MAX} with n. This is illustrated in Fig. 11a). Furthermore, an almost linear decrease of the FPZ size with increasing strain hardening exponent is found. However, when the same plot is made in Fig. 10e) as a function of X/δ, one finds that the plastic strain fields match to one another very well at the same value of δ. This indicates that the local plastic strain field is to first order geometrically controlled by the degree of blunting. Finally, Fig. 11b) represents the computed Shih factor dependency on n, which namely decreases with increasing n. The evolution of δ is computed by tracking the displacement of the points on the crack faces connected to the crack tip by two straight lines that form an angle of 45° with the crack tip in the current configuration. After the initial decrease with increasing applied J (red zone in Fig. 11b)) which is due to the fact that δ is not respecting condition (36), d_n converges to the value originally computed by C. F. Shih, here represented by the dotted line for $n = 0.3$, $n = 0.5$, while for $n = 0.01$ and $n = 0.1$ there is a 30% and 23% difference respectively.

3.2. *Gurson based simulations*

3.2.1. *Void cell simulations*

In order to produce reliable predictions with the nonlocal Gurson model, one needs to fine-tune the adjustment parameters q_1, q_2 of Eq. (16), the parameters α and β of the Thomason constraint factor C_{Tf} of Eq. (22), and κ which controls the evolution of the void spacing in Eq. (18) and Eq. (25).

Void cell simulations were performed for this purpose with J_2 plasticity by considering an axisymmetric model with a void located at its center corresponding to an initial porosity f_0. This is an approximation with respect to the plane strain condition addressed in this work, see Scheyvaerts et al. (2011) for 3D cell calculations under plane strain conditions. Nevertheless, the impact is limited as only moderate to large stress triaxialities are considered in this study and only minor effects on void shape evolution are expected when comparing axisymmetric and plane strain cases with respect to void growth. Fig. 12 illustrates the axisymmetric geometry with the considered spatial discretization and the void. Different values of the stress triaxiality were applied, namely $T = 0.75$, $T = 1$, $T = 1.5$, $T = 2$, and $T = 3$. Then, the results are fitted by the advanced Gurson model described in Section 2 under the same loading conditions, minimizing their differences, i.e., performing an optimization process. Fig. 13 shows the result of the optimization process in terms of the evolution of the equivalent Von Mises stress and porosity as a function of the normalized plastic dissipation energy for a material with $n = 0.3$ and $f_0 = 10^{-2}$. There is a near-perfect agreement between the results of the unit cell simulations and those of the nonlocal Gurson model across all values of stress triaxiality.

The values of the parameters for different values of the initial porosity f_0 and strain hardening exponent n are reported in Table 1.

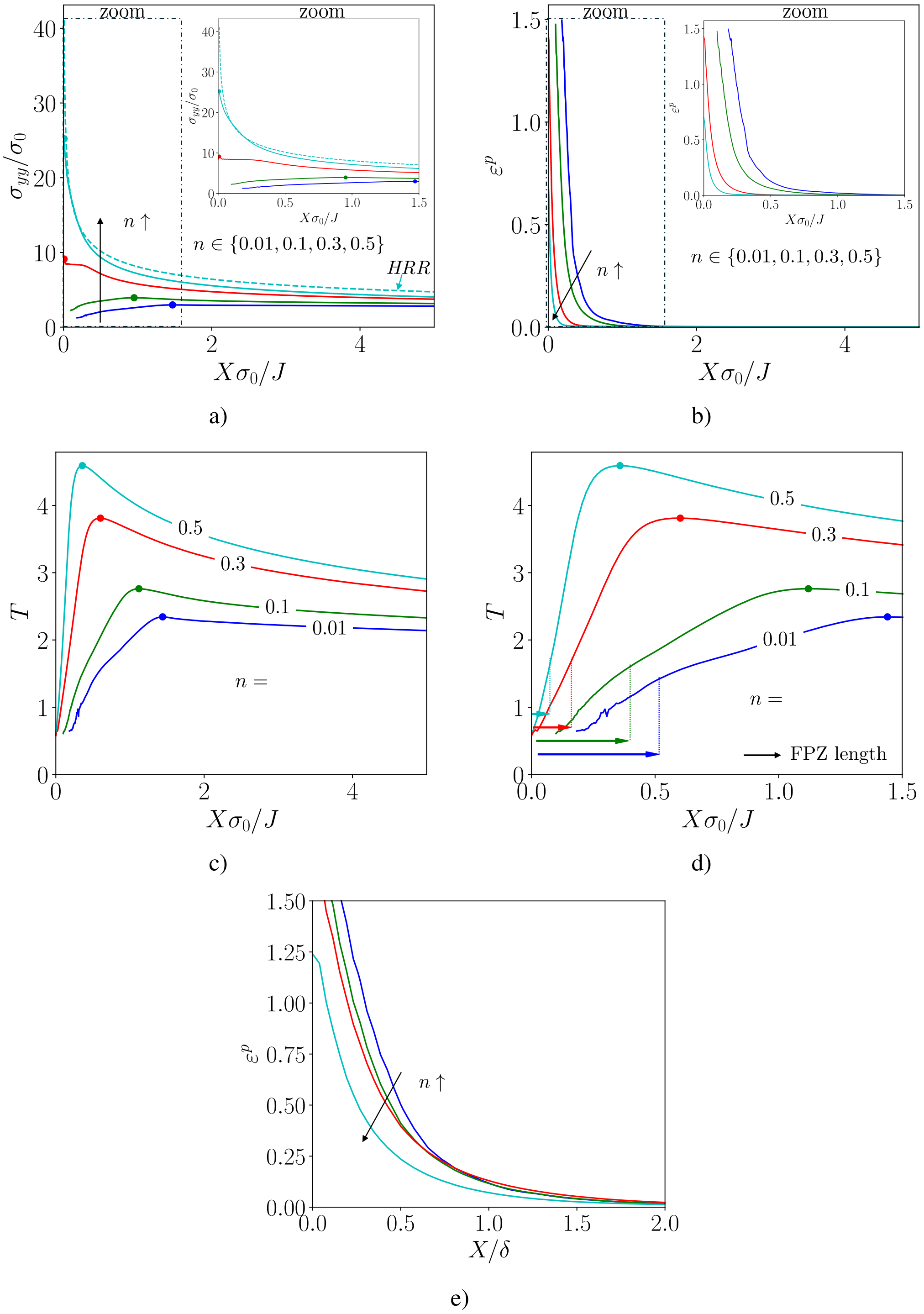

Figure 10: Results from the SSY simulations using the J_2 elastoplastic model for various strain hardening exponents and $k = 666$: a) Variation of the opening stress and HRR solution with respect to the normalized position; b) Accumulated plastic strain as a function of the normalized position; c) Stress triaxiality as a function of the normalized position; d) Stress triaxiality as a function of the normalized position and FPZ length; e) Accumulated plastic strain as a function of the position normalized by the crack tip opening.

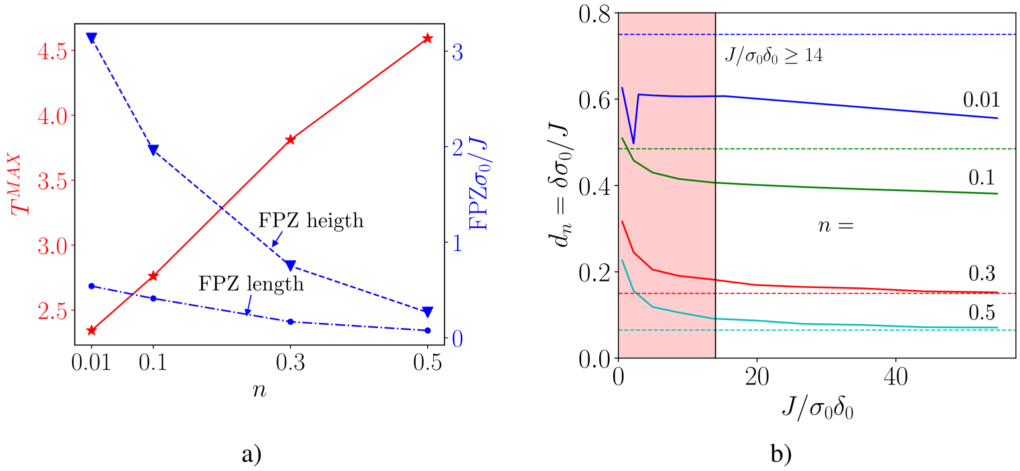

Figure 11: Results from the SSY simulations using the J_2 elastoplastic model for various strain hardening exponents and $k = 666$: a) Maximum stress triaxiality and fracture process zone (FPZ) length and height for $J/\sigma_0\delta_0 \approx 20$; b) Variation of the Shih factor as a function of the normalized applied J and comparison with the value originally computed by Shih.

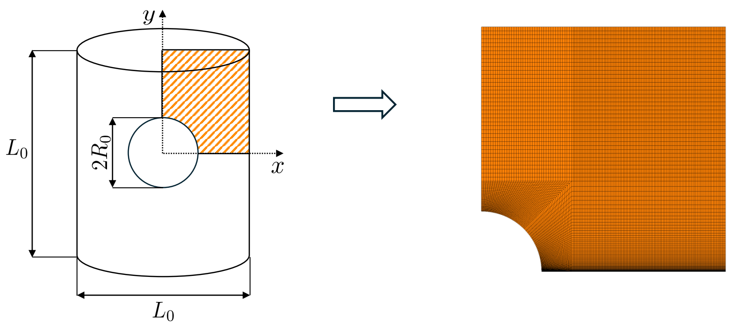

Figure 12: Axisymmetric cylindrical void cell (left) and corresponding axisymmetric finite element mesh used to calibrate the parameters of the advanced Gurson model.

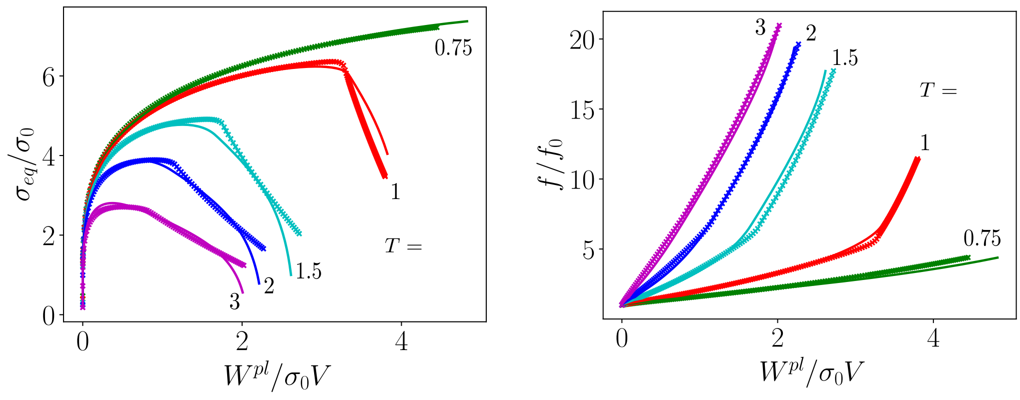

a) b)

Figure 13: Results of the optimization process for different values of stress triaxiality in a material characterized by $n = 0.3$ and $f_0 = 10^{-2}$. a) Evolution of the Von Mises stress as a function of the normalized plastic dissipation energy. b) Evolution of porosity as a function of the normalized plastic dissipation energy.

Table 1: Gurson-Thomason parameters dependence on f_0, n and k.

k	f_0	n	q_1	q_2	κ	α	β
666	10^{-3}	0.5	1.111	0.928	1.487	0.017	1.909
	10^{-2}	0.5	1.559	0.821	1.481	0.073	1.798
	$5 \cdot 10^{-2}$	0.5	1.386	0.867	1.070	0.413	1.702
	10^{-3}	0.3	1.103	0.966	1.496	0.286	1.551
	10^{-2}	0.3	1.161	0.949	1.487	0.353	1.520
	$5 \cdot 10^{-2}$	0.3	1.325	0.914	0.821	1.045	1.279
	10^{-3}	0.1	1.317	0.993	1.492	0.320	1.185
	10^{-2}	0.1	1.018	1.067	1.147	0.366	1.195
	$5 \cdot 10^{-2}$	0.1	1.196	1.027	0.249	0.995	0.919
	10^{-3}	0.01	1.358	1.047	1.426	0.280	1.078
	10^{-2}	0.01	1.115	1.089	0.666	0.401	0.965
	$5 \cdot 10^{-2}$	0.01	1.383	0.960	0.139	0.608	0.944
200	10^{-3}	0.5	1.342	0.842	1.495	0.024	1.920
	10^{-2}	0.5	1.388	0.839	1.493	0.234	1.804
	$5 \cdot 10^{-2}$	0.5	1.396	0.842	1.027	0.603	1.709
	10^{-3}	0.3	1.555	0.855	1.497	0.268	1.465
	10^{-2}	0.3	1.183	0.929	1.491	0.278	1.564
	$5 \cdot 10^{-2}$	0.3	1.321	0.909	0.732	1.206	1.235
	10^{-3}	0.1	1.240	0.983	1.059	0.373	1.138
	10^{-2}	0.1	1.001	1.057	1.152	0.301	1.271
	$5 \cdot 10^{-2}$	0.1	1.101	1.059	0.170	1.280	0.838
60	10^{-3}	0.5	1.292	0.852	1.495	0.022	1.943
	10^{-2}	0.5	1.324	0.854	1.500	0.211	1.832
	$5 \cdot 10^{-2}$	0.5	1.368	0.848	1.044	0.422	1.760
	10^{-3}	0.3	2.051	0.775	1.495	0.447	1.226
	10^{-2}	0.3	1.148	0.942	1.480	0.308	1.554
	$5 \cdot 10^{-2}$	0.3	1.272	0.923	0.786	0.898	1.332
	10^{-3}	0.1	1.178	1.002	0.934	0.447	1.023
	10^{-2}	0.1	1.002	1.063	1.117	0.282	1.274
	$5 \cdot 10^{-2}$	0.1	1.147	1.033	0.211	1.077	0.922

3.2.2. SSY simulations with Gurson model

Table 2 gathers all the parameters used for the Gurson-based SSY simulations. Fig. 14 presents the J_R curves for three different initial porosities, namely $f_0 = 5 \cdot 10^{-2}$ (Fig. 14a)), $f_0 = 10^{-2}$ (Fig. 14b)), and $f_0 = 10^{-3}$ (Fig. 14c)), and $k = 666$. The slope of the blunting line increases with the strain hardening exponent. In Fig. 14c) for $n = 0.01$ and $n = 0.1$, the simulation was halted once the crack had propagated multiple nonlocal lengths due to very small time increments. The primary quantity of interest that can be derived from the J_R curves in Fig. 14 is the fracture toughness, which serves as the central focus of the study. J_{Ic} increases markedly with increasing n and decreasing f_0.

Table 2: Material parameters used in the simulations.

Elastoplastic parameters	$E/\sigma_0 = 666$, $k = 60, 200, 666$, $\nu = 0.3$, $n = 0.01, 0.1, 0.3, 0.5$
Initial void characteristics	$f_0 = 10^{-3}, 10^{-2}, 5 \cdot 10^{-2}$, $\lambda_0 = 1$
Porosity related parameters	q_1 (see Table 1), q_2 (see Table 1), $A_n = 0$, $k_\omega = 0$,
	κ (see Table 1), α (see Table 1), β (see Table 1),
Nonlocal parameters	$l_{nl} = \delta_0$

Fig. 15 shows the variation of the fracture toughness J_{Ic} as a function of f_0 for different n and k, see Table 3a which collects all J_{Ic} values. The effect of the initial porosity is more pronounced for materials with very high strain hardening capacity. The tearing modulus is another key parameter that can be extracted from the J_R curve. Fig. 16 shows that the tearing modulus $T_J = \Delta J/(\sigma_0 \Delta a)$ increases with n consistently across different initial porosity values. Furthermore, materials with a lower f_0 exhibit a higher tearing modulus for the same strain hardening capacity. Here, T_J is computed at each consecutive time increment, with the final value obtained as the average overall increments.

Alternatively, another normalization approach for J could account for strain hardening by using a mean flow stress σ_{Ym} calculated as the average between the initial yield stress and true strength at necking σ_{Cn}. The Considère criterion is used to derive the true stress at the Considère point σ_C and the corresponding nominal stress R_m

Table 3: Normalized FT values using (a) the initial yield stress and (b) the mean flow stress, for different strain hardening parameter n, initial porosity f_0, and k.

(a) $J_{Ic}/\sigma_0 l_{nl}$

n	k	f_0: $5 \cdot 10^{-2}$	10^{-2}	10^{-3}
0.01	666	0.24	3.48	8.04
0.1	666	1.62	6.98	15.63
0.3	666	13.65	32.80	69.10
0.5	666	78.62	136.30	284.66
0.1	200	1.60	6.69	18.45
0.3	200	10.05	20.76	43.81
0.5	200	42.60	75.38	166.42
0.1	60	1.28	6.07	16.02
0.3	60	5.48	15.05	30.71
0.5	60	20.21	39.45	85.31

(b) $J_{Ic}/\sigma_{Ym} l_{nl}$

n	k	f_0: $5 \cdot 10^{-2}$	10^{-2}	10^{-3}
0.01	666	0.23	3.45	8.00
0.1	666	1.37	5.87	13.14
0.3	666	5.89	14.16	29.80
0.5	666	13.03	22.58	47.17
0.1	200	1.44	6.02	16.60
0.3	200	5.69	11.76	24.80
0.5	200	12.04	21.34	47.10
0.1	60	1.22	5.82	15.38
0.3	60	3.95	10.89	22.21
0.5	60	9.34	18.25	39.48

$$R_m \approx \sigma_0 \, (kn)^n \exp(-n) \tag{38}$$

to compute

$$\sigma_{Ym} = \frac{1}{2} \left(\sigma_0 + R_m \right) . \tag{39}$$

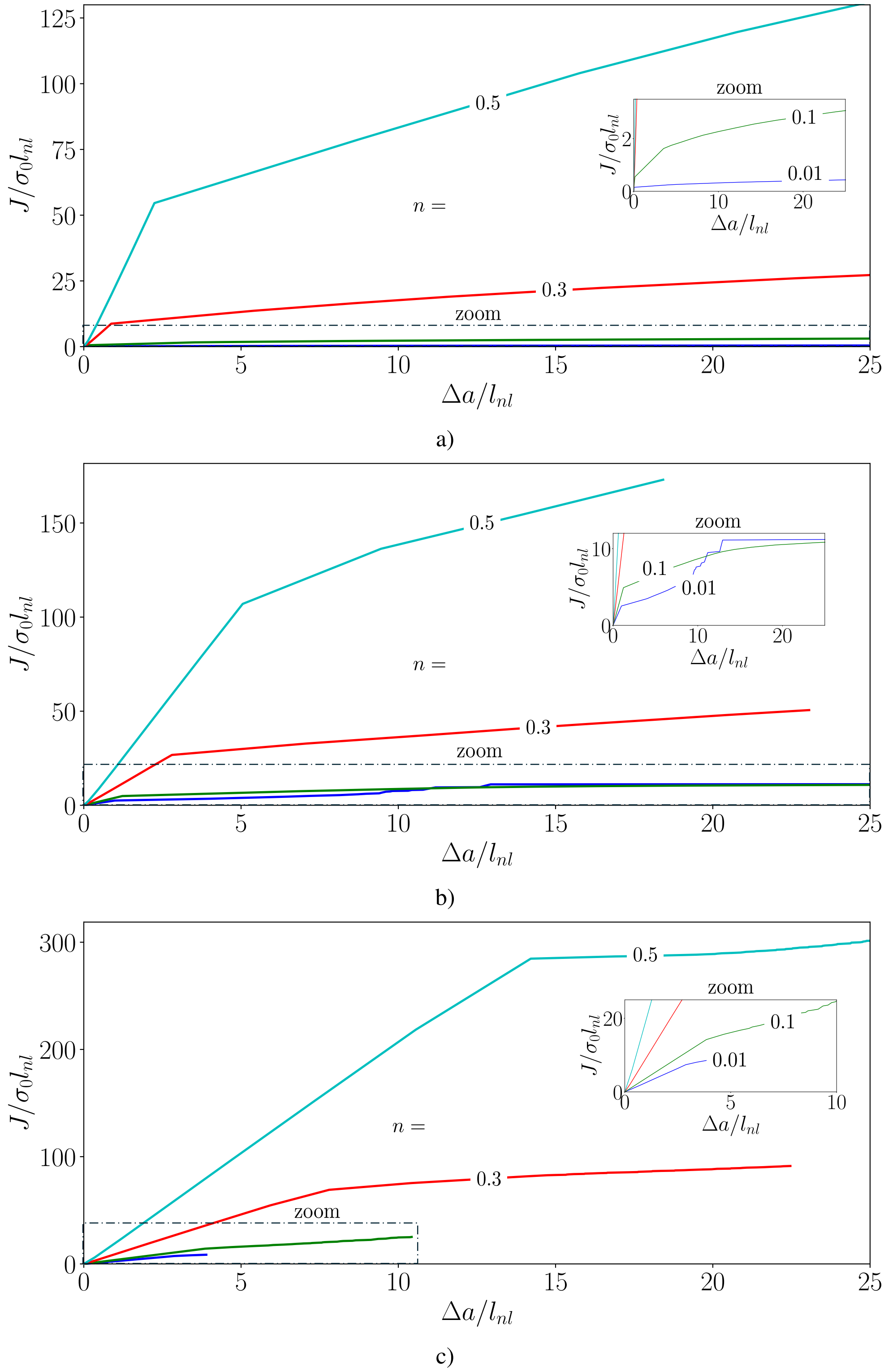

Figure 14: J_R curves predicted by the nonlocal Gurson model as a function of the strain hardening exponent (k = 666) for different values of the initial porosity f_0: a) $f_0 = 5 \cdot 10^{-2}$; b) $f_0 = 10^{-2}$; c) $f_0 = 10^{-3}$.

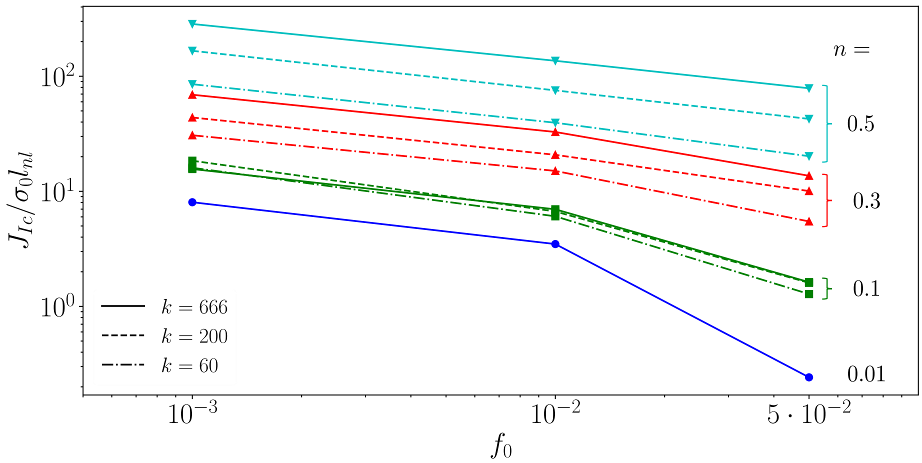

Figure 15: Fracture toughness predicted by the nonlocal Gurson model (normalized by yield stress and nonlocal length) as a function of the initial porosity f_0, for different strain hardening exponent and k parameter.

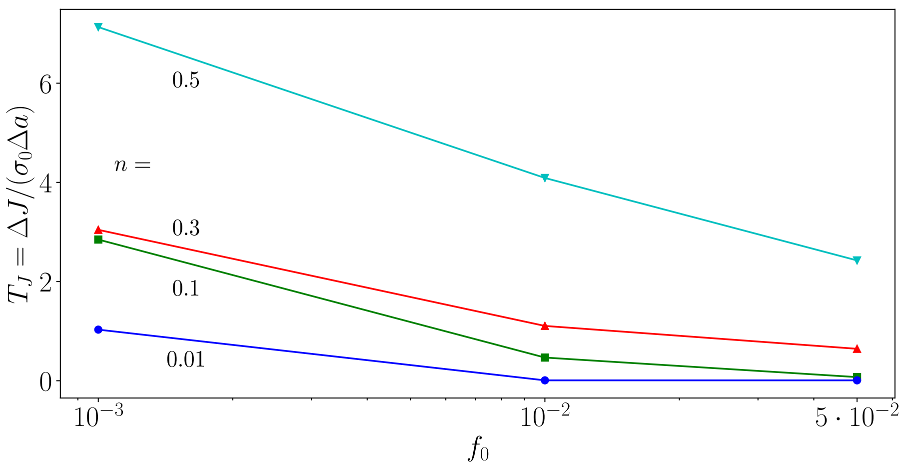

Figure 16: Tearing modulus associated with the J_R curves predicted by the nonlocal Gurson model as a function of the initial porosity f_0, for different strain hardening exponent with $k = 666$.

Fig. 17 presents this new normalized fracture toughness as a function of the initial porosity and strain hardening exponent. Although the variations with n are reduced, the trend aligns with that of Fig. 15a). The FT values are reported in Table 3b.

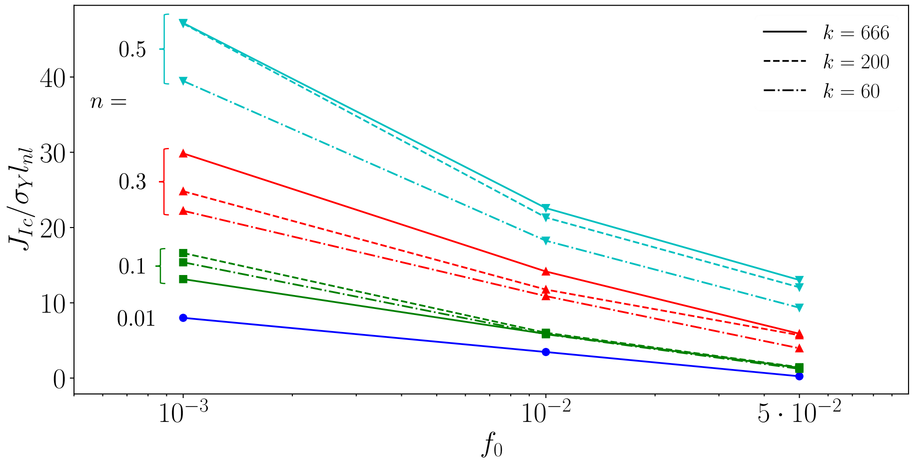

Figure 17: Fracture toughness normalized by $\sigma_{Ym} l_{nl}$ predicted by the nonlocal Gurson model as a function of the initial porosity f_0, for different strain hardening exponent and k parameter.

The influence of the strain hardening is further highlighted by considering the critical crack tip opening displacement δ_c.

Fig. 18a) depicts the variation of critical crack tip opening displacement normalized by l_{nl}. The value increases with n but much less than for J_{Ic}. This result comes directly from the low Shih factor d_n at high n. Specifically, materials with lower initial porosity exhibit a higher δ_c. Fig. 18b) shows the same results but with δ_c normalized by $l_{nl}\exp(\varepsilon_c^p)$, for $f_0 = 10^{-3}$ and $f_0 = 10^{-2}$. This shows that as a first approximation δ_c can be approached by a rough estimate of the extension of a slab of initial thickness l_{nl} deformed by ε_c^p.

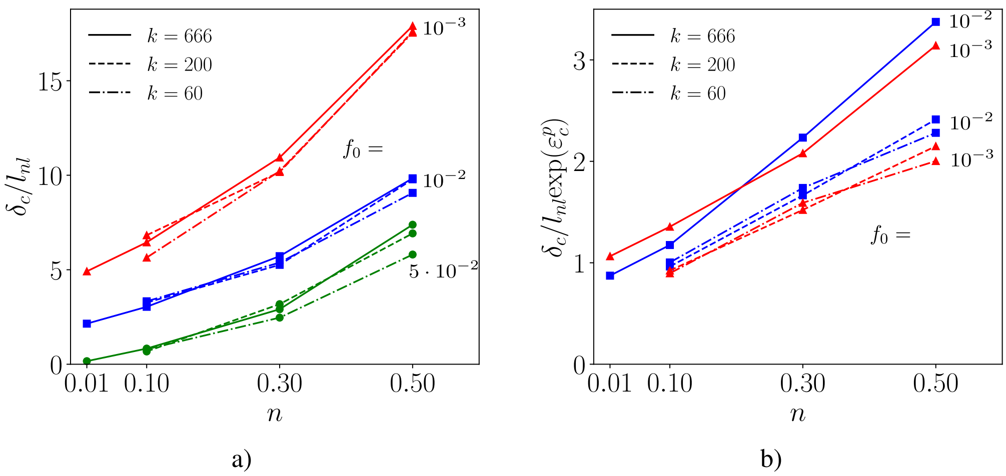

Figure 18: Variation of the critical crack tip opening displacement as a function of the strain hardening exponent n for different values of the initial porosity f_0 and k.

Fig. 19 illustrates the ligament size ratio distribution as a function of the strain hardening exponent n for $f_0 = 10^{-2}$. For $n = 0.01$, the crack branches into two sub-cracks, while the other values of n lead to a straight crack propagation. This specific response, probably a numerical artifact, for $n = 0.01$ has not been investigated further in this study. Fig. 19 also highlights the different crack propagation angles, increasing with n.

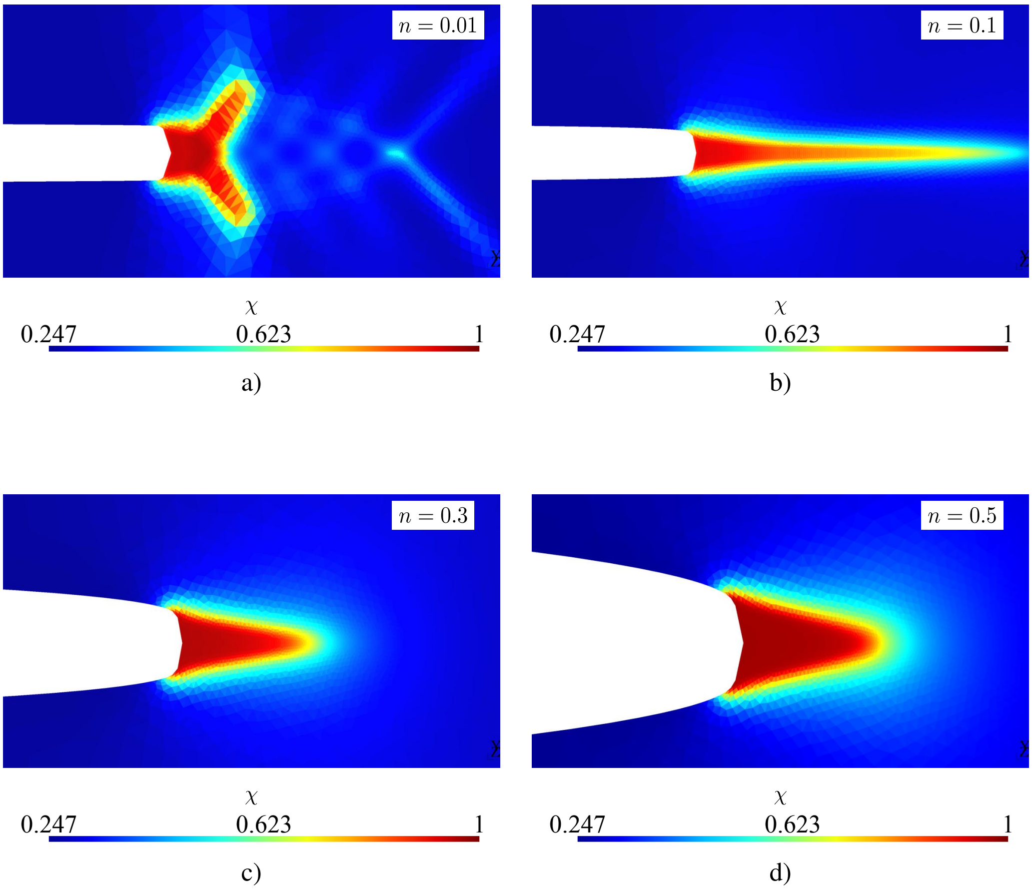

Figure 19: Ligament size ratio distribution ahead of the crack tip for an initial porosity of $f_0 = 10^{-2}$ and different values of the strain hardening n: a) $n = 0.01$; b) $n = 0.1$; c) $n = 0.3$; d) $n = 0.5$.

Finally, Fig. 20 shows a) the porosity evolution as a function of the accumulated plastic strain and b) the variation of the accumulated plastic strain as a function of stress triaxiality for a point on the ligament located at distance $X/l_{nl} = 1$. The evolution of these quantities is plotted until the onset of cracking. Some other distributions at other positions ahead of the crack tip can be found in Appendix B. Fig. 20 a) illustrates that for $X/l_{nl} = 1$, a lower porosity rate is found with increasing n. Regarding the accumulated plastic strain at fracture, Fig. 20 b) shows that it increases with n. The loading path appears to be not much dependent on the strain hardening, indicating again that the geometry of the blunting process dominates the crack initiation process. Materials with higher strain hardening capacity fail at higher values of accumulated plastic strain as they tend to undergo lower stress triaxiality on average in the loading history, even though the maximum stress triaxiality is larger. Additionally, a higher n tends to delay void coalescence.

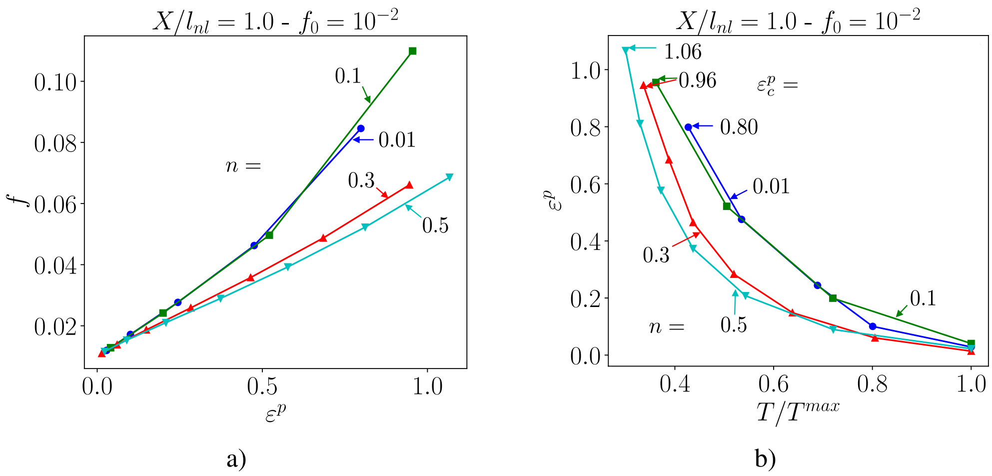

Figure 20: Evolution of several quantities of interest at a location $X = l_{nl}$ ahead of the crack tip up to cracking initiation. a) Porosity evolution as a function of the accumulated plastic strain; b) variation of accumulated plastic strain evolution as a function of the stress triaxiality.

3.2.3. Effect of the Gurson-Thomason parameters adjustment on crack propagation

The fitting parameters q_1, q_2, κ, α, β were calibrated using void cell calculations, as a function of the initial porosity, strain hardening exponent and k value. Some works in the literature calibrate the two parameters q_1 and q_2 with the strain hardening. One example can be found in the study of Faleskog et al. (1998), where the authors proposed a calibration of q_1, q_2 based on void cell simulations. Fig. 21 illustrates the dependence of J_{Ic} on q_1, q_2, κ, α, and β, showing the importance of properly fine tuning these parameters. As a matter of fact, the fracture toughness and the tearing modulus significantly change when comparing the simulations performed with or without adjusting the parameters. The effect of modifying the fitting constants on the FT is more pronounced for high values of the strain hardening exponent.

3.2.4. Effect of void nucleation

Although a comprehensive analysis of void nucleation effects would require an entire study per se depending on the mechanism of nucleation that is considered, we present a preliminary set of results based on the strain-based criterion from Chu and Needleman (1980), as outlined in Eq. (19). This analysis aims to assess the impact of delayed void nucleation on the fracture toughness. We consider a material with a strain hardening exponent of $n = 0.1$, a volume fraction of inclusions $f_N = 10^{-2}$, and three different values of nucleation strain ε_N set at 0.05, 0.1, and 0.15, with s_N fixed at 0.01 which means a very narrow "burst" type nucleation. Fig. 22a) shows that, as expected, a higher nucleation strain increases the resistance to cracking. The FT associated with a material with $f_N = 10^{-2}$ is higher than the one of a material with an initial porosity of 10^{-2} with no void nucleation. Specifically, FT increases by a factor of 1.3, 1.5, 1.6 for ε_N equal to 0.05, 0.1, and 0.15, respectively. Fig. 22b) illustrates the porosity evolution at a point situated at a distance of one nonlocal length from the initial crack tip as a function of the accumulated plastic strain. For the three values of ε_N, one can see the sudden increase of porosity around the strain at which voids are nucleated.

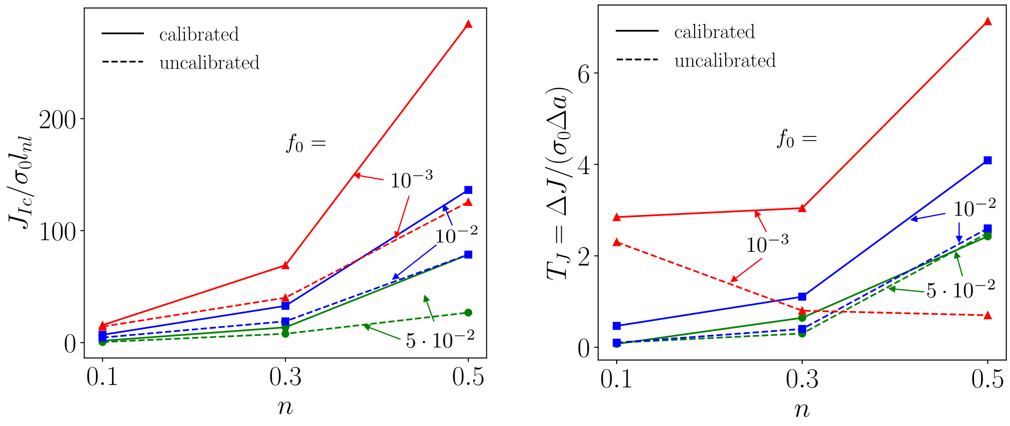

a) b)

Figure 21: Effect of fine-tuning the Gurson-Thomason parameters $q_1, q_2, \kappa, \alpha, \beta$ on: a) the FT; b) the tearing modulus for different strain hardening exponent and porosity.

Then, once voids are fully nucleated, i.e., $f = f_N$, porosity grows fast because of the high-stress triaxiality in front of the crack until rupture.

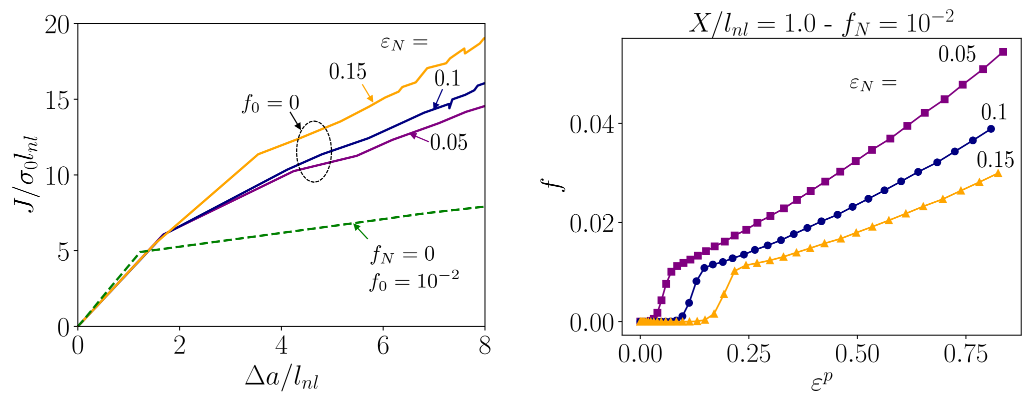

a) b)

Figure 22: Effect of void nucleation for three nucleation strains ε_N and $f_N = 10^{-2}$. a) J_R curves; b) porosity evolution as a function of the accumulated plastic strain at a position ahead of the crack equal to l_{nl}.

4. Discussion

4.1. Comparison/validation with literature and meaning of l_{nl}

The SSY model has already been applied in other studies to investigate the ductile tearing resistance of metals. In the earlier investigation by Pardoen and Hutchinson (2003), different strain hardening exponents were considered, with different initial porosity. The results for $n = 0.01$, $n = 0.1$, and $n = 0.2$ are compared in Fig. 23a) to those of Pardoen and Hutchinson (2003), considering $f_0 = 10^{-3}$ and $f_0 = 10^{-2}$. The ratio between the normalized FT $J_{Ic}/\sigma_0 l_{nl}$ and the one of Pardoen & Hutchinson $J_{Ic}^{PH}/\sigma_0 X_0$ where X_0 is the element size assumed to be equal to the void spacing, for the same value of n is not constant with decreasing initial porosity. This difference is larger for $n = 0.01$ and $n = 0.1$. This comparison indicates that l_{nl} should be taken as equal to $X_0/6 \rightarrow X_0/3$ to adjust the results to one another.

Note that Pardoen and Hutchinson (2003) found that their results matched very well with simulations including voids introduced in a discrete manner in a FE mesh when taking X_0 as the void spacing in the discrete voids calculations. Now, the two models are different. First, the present model is nonlocal. Second, in Pardoen and Hutchinson (2003), the Gologanu-Leblond-Devaux model (Gologanu et al., 1993) with void shape effect was employed together with the Thomason for void coalescence. Hence, care should be taken to consider this comparison as a definitive conclusion that l_{nl} is equal to 1/6 to 1/3 of X_0 but it gives a first idea of the connection of l_{nl} to a physical dimension.

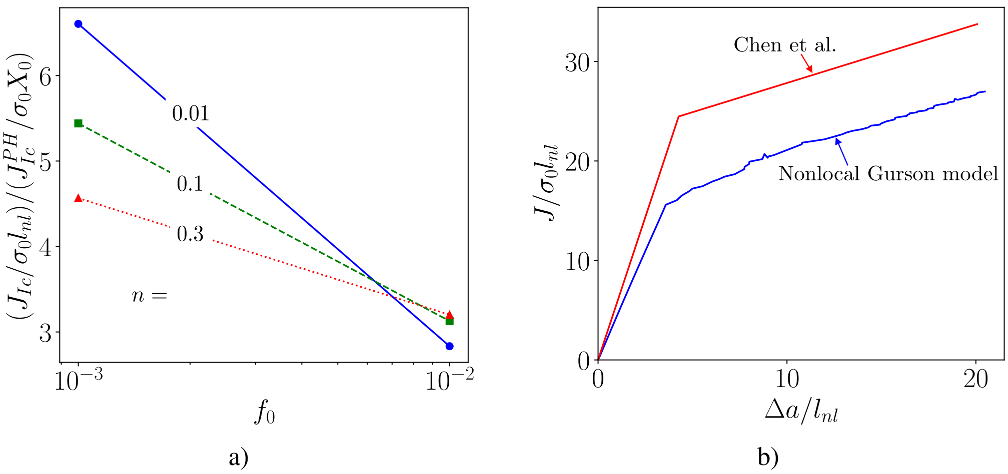

Figure 23: Comparison of the J_{Ic} and J_R curves with literature: a) J_{Ic} value comparison with the results of Pardoen and Hutchinson (2003); b) J_R curve comparison with the results of Chen et al. (2020).

As already mentioned, another study employing the SSY framework is that of Chen et al. (2020). Fig. 23b) shows the J_R curves for $n = 0.15$ and $f_0 = 10^{-3}$ predicted with the two models. Comparable tearing modulus and blunting slope are found. The largest difference concerns the FT and the onset of cracking. It is worth recalling that although the model of Chen et al. (2020) is also nonlocal, the methodology used to compute the crack length is based on the notion of a maximum porosity at fracture f_F, while here a description fully based on the micromechanics of void coalescence is adopted. Nevertheless, the two models can be considered very similar.

4.2. Effect of strain hardening on J_{Ic}

The effect of the strain hardening capacity on FT is the core subject of this study aimed at understanding why strain hardening has such a major positive impact on J_{Ic}. The results from Figs. 20a) and 20b) are summarized in Fig. 24. Fig. 24 presents a) the accumulated plastic strain and b) the porosity at failure as a function of the strain hardening exponent for different f_0 and k. Near the crack tip, the values of ε_c^p and f_c are consistently larger than those found further from the crack tip across all combinations of f_0 and n. The critical accumulated plastic strain increases with n, with a more pronounced increase for $f_0 = 10^{-3}$. The strain at failure is not significantly influenced by the strain hardening exponent nor by the critical porosity. Hence, the large FT at high n has another origin, which is discussed hereafter.

Different criteria have been proposed to predict ductile cracking initiation. Following Rice's approach, a very simple first possible fracture criterion could be based on the critical crack tip opening displacement δ_c to be large enough that the large strain zone encompasses a region larger than the void spacing, i.e.

$$\delta_c = \mu X_0 \tag{40}$$

with μ a constant of order one, and X_0 the void spacing. One could thus assume that as soon as Eq. (40) is verified, fracture starts. Fig. 11b) demonstrates that, for a given μX_0, a higher J is necessary to reach the same δ as the value of n increases, which explains the higher J_{Ic} found in materials with larger strain hardening capacity.

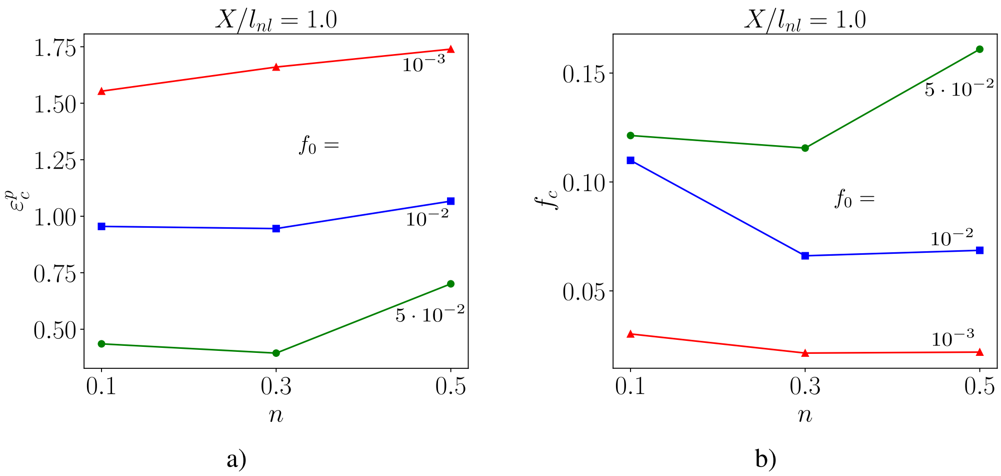

Figure 24: Quantities of interest at failure as a function of the strain hardening exponent and the initial porosity: a) accumulated plastic strain; b) porosity.

A second uncoupled local approach model is based on the attainment of a critical value of the accumulated plastic strain, ε_c^p, which writes

$$\varepsilon^p(X) = \varepsilon_c^p. \tag{41}$$

Cracking initiates once the material reaches at a certain distance X_0 from the crack tip a critical level of accumulated plastic strain. Fig. 25a) demonstrates that the critical accumulated plastic strain is reached at much higher loads for larger n, leading to higher values of J_{Ic}. Take a given distance $X = X_0$, Fig. 25a) shows that the plastic strain is much smaller at the same level of J when n increases. Fig. 25b), which is another way of representing Fig. 25a), shows the variation of J_{Ic} for different values of the critical accumulated plastic strain. Fig. 25c) also illustrates that for a given value of ε_c^p, J_{Ic} increases with n, with a more noticeable difference for high values of ε_c^p. Increasing ε_c^p has a more pronounced effect on the J_{Ic} for materials with high strain hardening. If one takes into account the results shown in Fig. 24 with slightly increasing ε_c^p with increasing n, this would only amplify the trends depicted in Fig. 25c).

Finally, based on Fig. 11a), one could already deduce that the effect of strain hardening on the FPZ size might explain the strain hardening dependency of the J_{Ic}. Assuming a distribution of voids with the nearest void located at a distance X_0, and further assuming that fracture occurs as soon as the FPZ engulfes this void, it becomes evident that for the same load, a higher strain hardening capacity leads to a shorter FPZ, which may not extend far enough to incorporate the void and higher loading is needed for crack initiation. Ultimately, the fundamental reason is partly hidden in the Shih factor, in the connection between δ and J. A higher n leads to a lower Shih factor, and a much higher J is needed to reach the same opening δ. At the end of the day, δ controls the damage growth much more than J as indicated with Fig. 18.

In conclusion, the three different simple ductile fracture criteria applied to the results of J_2 static crack simulations provide an insight into why materials with high values of strain hardening exhibit a higher fracture toughness. Obviously, the predictions with the Gurson model are more precise and lead to the same conclusion.

4.3. Ultra high opening stress peak

At this stage, one must pose the question of the validity of using a power law up to strains as large as 1 and with σ_{yy}/σ_0 reaching values up to 10 to 40 (see Fig. 10a)) or more for $n = 0.5$ (while the corresponding flow stress is about 10 to 25 σ_0 depending on k). More physical hardening laws are worth investigating in this context, such as those already proposed by Lecarme et al. (2011) and Nielsen et al. (2010) based on a Kocks-Mecking model with a stage IV hardening. This is left for further investigations.

The question is further complexified by the fact that strain hardening in some of these alloys is often partly or entirely the result of twinning or perhaps TRIP mechanisms. These mechanisms, such as forest hardening, exhaust at

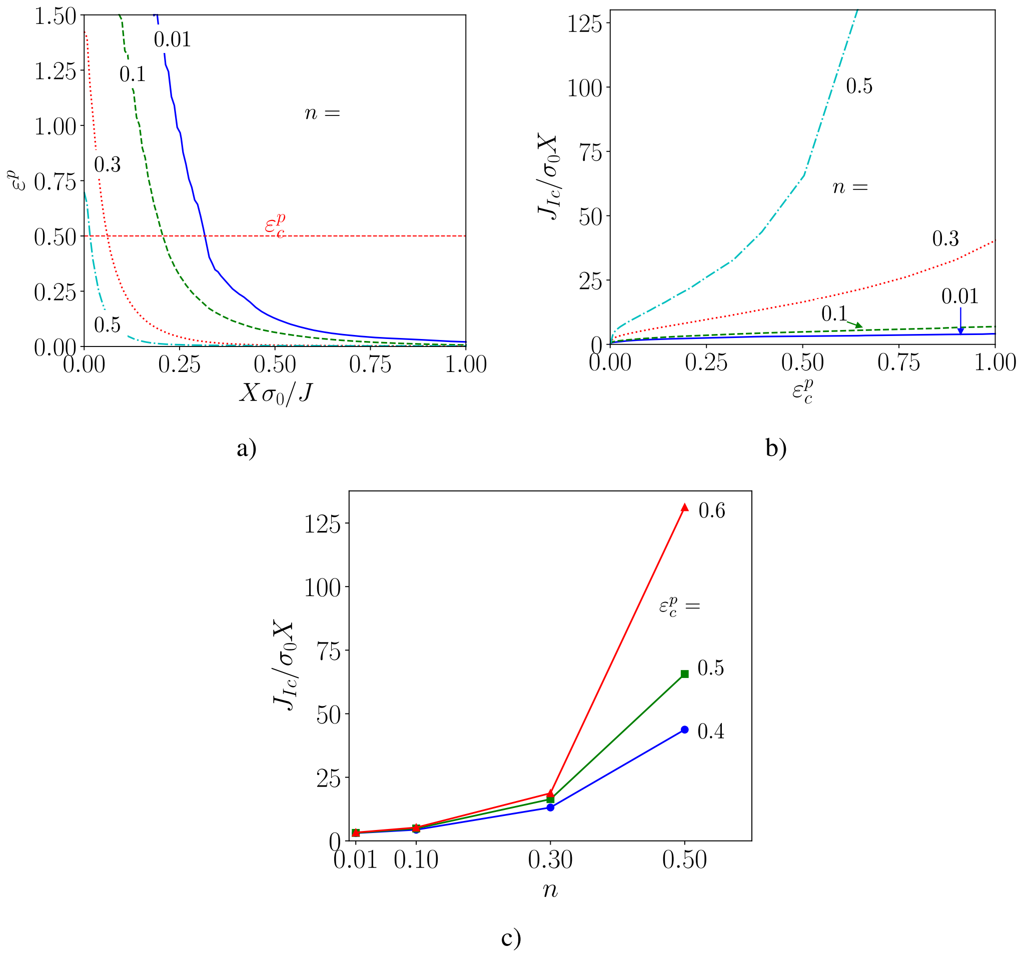

Figure 25: FT definition based on the critical value of the accumulated plastic strain for different values of the strain hardening exponent: a) variation of the accumulated plastic strain as a function of the normalized position; b) variation of FT as a function of the critical accumulated plastic strain; c) FT variation as a function of the strain hardening exponent for different critical plastic strains.

very large strains, making the power law representation invalid. Note that if other more sophisticated hardening laws are used, the parameters entering the Gurson model have to be readjusted, which is the subject of the next point of discussion.

A second element of attention is to consider the absolute magnitude of the stresses that are attained in the near crack tip region with very high values of n. Assuming power law hardening is valid up to strains of 1 or more, maximum principal stresses around 10-30σ_0 mean values above 3-9 GPa for instance for a stainless steel with $\sigma_0 = 300$ MPa. These are extremely large tensile stresses (which can be further amplified by very local stress concentrators related to grain boundaries, dislocation pile-ups, etc.). Such levels of stresses, approaching theoretical fracture stresses, become large enough to potentially promote other failure modes, such as intergranular failure (but after a significant amount of plastic deformation).

4.4. On the validity of Gurson model at large strain hardening

As previously explained, the fine-tuning as a function of n (and of f_0) of the parameters q_1, q_2 and of the other coalescence parameters is a necessity to generate accurate predictions. This was already recognized long ago by different authors (Faleskog et al. (1998), Pardoen and Hutchinson (2000), Benzerga and Leblond (2010)). The origin of this state of affairs is that the Gurson model has been derived in the context of perfect plasticity, while the introduction of strain hardening through Eq. (1) and a representative yield stress of the matrix material is a heuristic solution. A much more convincing solution, offered as a perspective of this work, is to implement a version of the Gurson model reworked to better deal with strain hardening. The work by Leblond et al. (1995) and recent extensions by Morin and colleagues (Roubaud et al., 2024; Bouby et al., 2023) are the only efforts, to our knowledge, along these lines. Ideally, such extensions should also be made in the context of using more physical hardening laws, such as a Kocks-Mecking model with stage IV hardening, as explained above.

5. Conclusions

This study explored the origin of the significant impact of strain-hardening capacity on the resistance to ductile crack growth. This also legitimates the research made in metallurgy to develop tougher alloys, such as stainless steels and modern alloys with the TRIP-TWIP effect and HEAs. J_2 plasticity-based and Gurson model-based nonlocal simulations show that increasing strain hardening leads to enhanced fracture toughness, J_{Ic}, and tearing resistance because of much lower plastic strains developing in front of the crack tip, hence later void coalescence. The effect on δ_c is much smaller, indicating that crack tip blunting primarily controls the growth of damage in the fracture process zone. The analysis also underscores the limitations of the Gurson model at high strain hardening, particularly the sensitivity to q_1 and q_2, α, β, and κ. As additional methodological messages, strict rules for the initial crack opening δ_0, mesh size, and SSY validity are set. These findings reinforce the potential of developing alloys with high strain-hardening capacity, offering not only improved tensile properties but also enhanced ductile fracture resistance.

Acknowledgements

This work has received funding from the European Research Council (ERC) under the European Union's Horizon 2020 research and innovation programme (Grant agreement No. 101097433), ERC advanced grant HAPI.

Computational resources have been provided by the supercomputing facilities of the Consortium des Équipements de Calcul Intensif en Fédération Wallonie Bruxelles (CÉCI) funded by the Fond de la Recherche Scientifique de Belgique (FRS-FNRS).

Appendix A. Mesh convergence study

Fig. A.26 shows the variation of the opening stress and stress triaxiality for two different meshes: the dashed line is the mesh employed in this work, and the continuous line represents a ten times finer mesh. No effect of mesh refinement is observed. As a matter of fact, for the continuous line, $l_e/\delta_0 = 0.03$ was used, whereas for the dashed line $l_e/\delta_0 = 0.3$. Conversely, with increased strain hardening to $n = 0.5$, Fig. A.27 illustrates that the coarser mesh ($l_e/\delta_0 = 0.3$) fails to capture both the peak stress and stress triaxiality near the crack tip. However, both meshes yield the same J_R curve, as shown in Fig. 7b). This indicates that a very fine mesh is necessary only to accurately resolve the opening stress distribution in the immediate vicinity of the crack tip.

The mesh dependency is predominant for high values of J yet almost negligible away from the crack tip. Fig. A.28 depicts the evolution of the accumulated plastic strain and confirms this trend and the difference between the results provided by the two meshes, with the coarser mesh that underestimates the true value of ε^p.

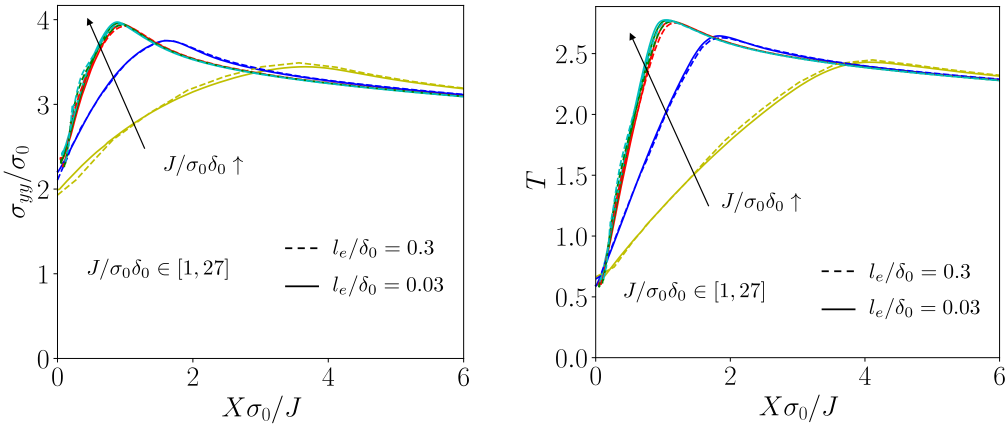

a) b)

Figure A.26: J_2 SSY simulations for $n = 0.1$ and $k = 666$ under different levels of loading characterized by the magnitude of $J/\sigma_0\delta_0$ and two different mesh refinements: $l_e/\delta_0 = 0.3$ and $l_e/\delta_0 = 0.03$. a) Opening stress as a function of the normalized position, b) Stress triaxiality as a function of the normalized position.

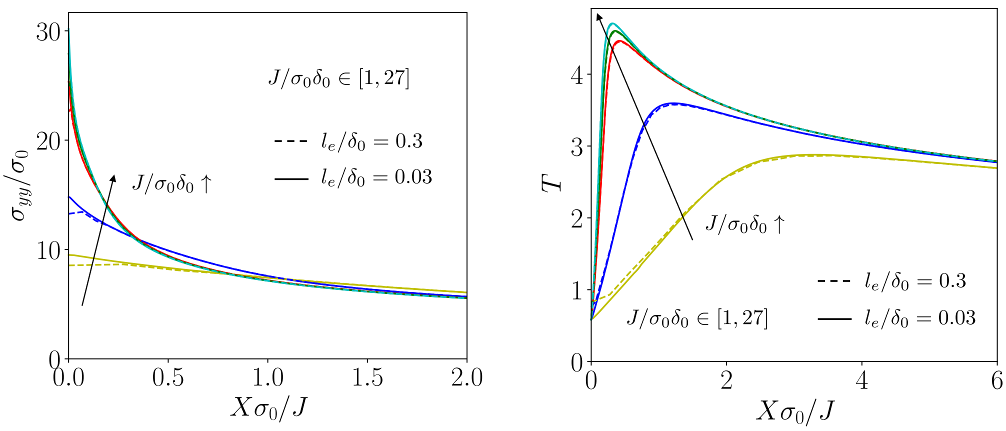

a) b)

Figure A.27: J_2 SSY simulations for $n = 0.5$ and $k = 666$ under different levels of loading characterized by the magnitude of $J/\sigma_0\delta_0$ and two different mesh refinements: $l_e/\delta_0 = 0.3$ and $l_e/\delta_0 = 0.03$. a) Opening stress as a function of the normalized position, b) stress triaxiality as a function of the normalized position.

Appendix B. Supplementary results on the SSY nonlocal Gurson model

Fig.B.29 provides extra data regarding the variation of the porosity as a function of the accumulated plastic strain at different fixed positions X/l_{nl} ahead of the crack tip. Figs. B.29a), B.29d), and B.29g) illustrate a comparable variation of the porosity as a function of the accumulated plastic strain when looking very close to the crack tip, with f

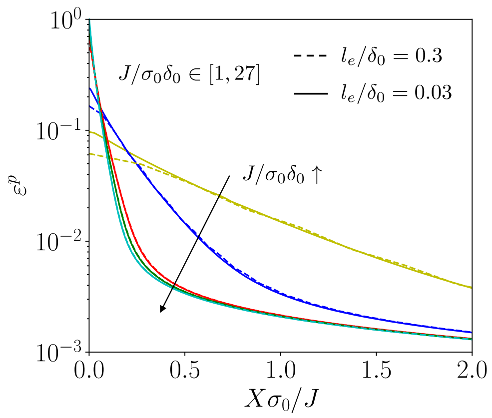

Figure A.28: J_2 SSY simulations for $n = 0.5$ and $k = 666$ under different levels of loading characterized by the magnitude of $J/\sigma_0\delta_0$ and two different mesh refinements: $l_e/\delta_0 = 0.3$ and $l_e/\delta_0 = 0.03$. Variation of the accumulated plastic strain as a function of the normalized position.

increasing with the strain hardening exponent. Then, Figures B.29b), B.29e), and B.29h) portray similar evolution of the porosity as a function of the accumulated plastic strain when moving further away from the crack tip at $X/l_{nl} = 5$. The sudden increase of f for $n = 0.01$ in Fig. B.29e) is due to crack branching that is not further investigated.

Finally, Figures B.29c), B.29f), and B.29i) highlight an opposite trend in the porosity rate that for the point furthest from the crack tip at $X/l_{nl} = 10$.

Figs.B.30 provide extra data on the variation of the accumulated plastic strain with respect to the corresponding stress triaxiality at different distances from the crack tip. This shows that a material element at a fixed point undergoes more or less the same plastic strain/triaxiality trajectory not much influenced by n. Fig. B.30a), B.30b), B.30c) demonstrate that close to the crack tip, the stress triaxiality decreases with increasing accumulated plastic strain, until rupture. On the other hand, Figures B.30d), B.30e), B.30f), B.30g), B.30h), and B.30i) show that when considering points further from the initial crack, the stress triaxiality increases, then decreases, until it reaches a plateau, while the accumulated plastic strain increases until rupture.

Appendix C. Influence of the initial crack opening

Fig. C.31 illustrates the effect of crack opening on the mechanical response. In terms of maximum opening stress (Fig. C.31a)), the initial crack tip opening δ_0 appears to have little influence, with only minor differences observed between the three curves near the crack tip. For the accumulated plastic strain, in Fig. C.31b) the curves nearly overlap, indicating that δ_0 has a negligible impact. Regarding the stress triaxiality and the fracture process zone (FPZ) length, a smaller δ_0 shifts the peak of the stress triaxiality closer to the crack tip, though the absolute values and FPZ length remain essentially unchanged. Then, Fig. C.32a) shows that a higher initial crack opening involves a higher crack tip opening displacement. Furthermore, the dependency of the crack tip opening displacement on δ_0 is more evident for $J/\sigma_0\delta_0 > 8.7$ (where $\delta_0 = 0.1$ mm was employed). When applying the nonlocal Gurson model, we primarily focus on the J_R curve. For a material with $n = 0.3$ and $f_0 = 10^{-2}$, Fig. C.32b) illustrates that the initial crack tip opening δ_0 does not significantly affect the blunting line or the FT value. Although a slight difference is found during crack propagation, with a 10% difference in terms of the FT when considering $\delta_0 = 0.02$ mm and $\delta_0 = 0.06$ and 0.1 mm, all the results exhibit similar tearing moduli.

Appendix D. Comparison with other FE model

To validate the ultra-high opening stress peak described in the previous sections, a comparison was performed with the code Zebulon of the Z-set suite, see Besson and Foerch (1997), for an elastoplastic material with a strain hardening exponent of $n = 0.5$. The present model was evaluated using two different mesh sizes, as detailed in the

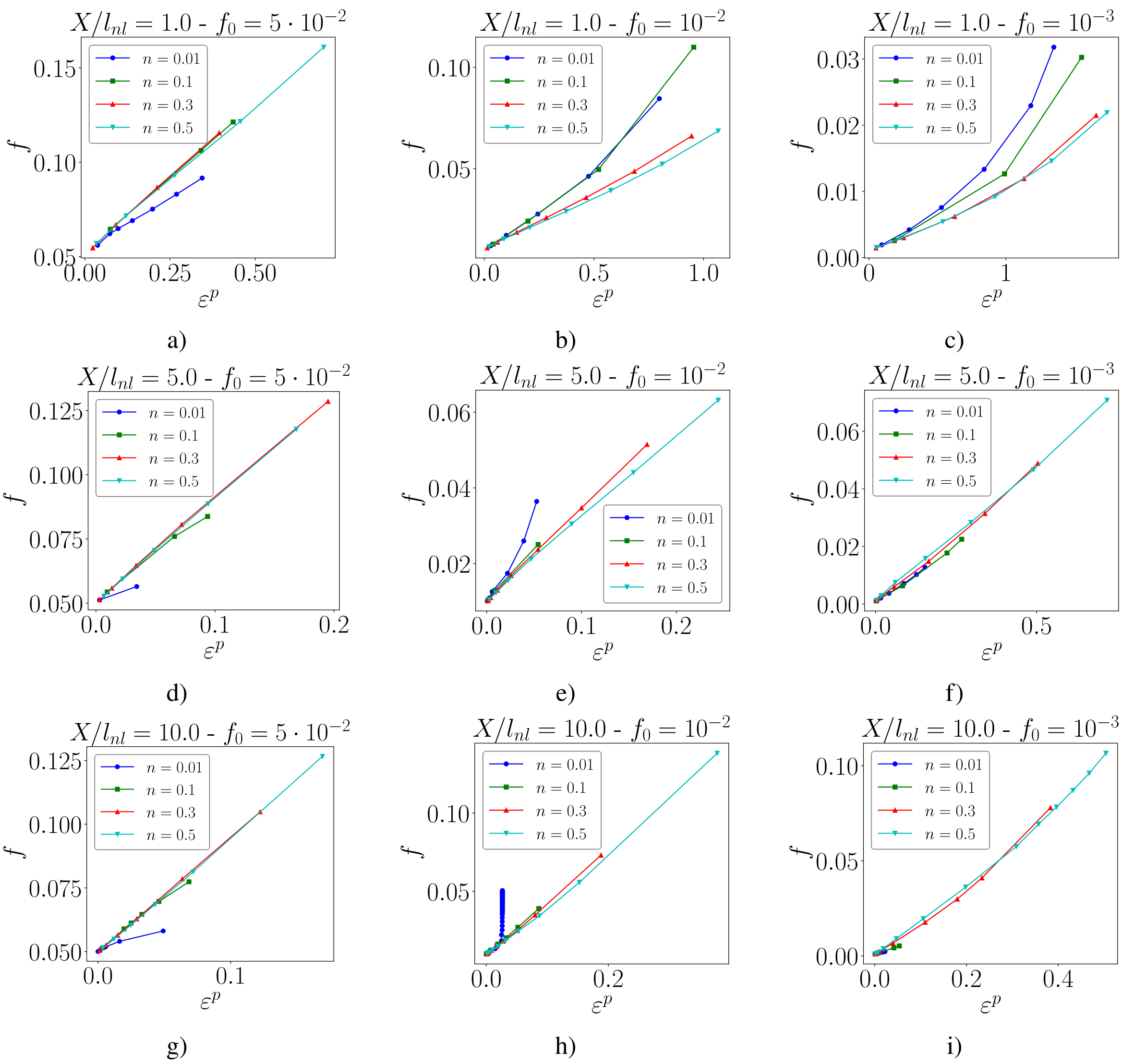

Figure B.29: Porosity evolution as a function of the accumulated plastic strain at three different distances X from the crack tip normalized by l_{nl}.

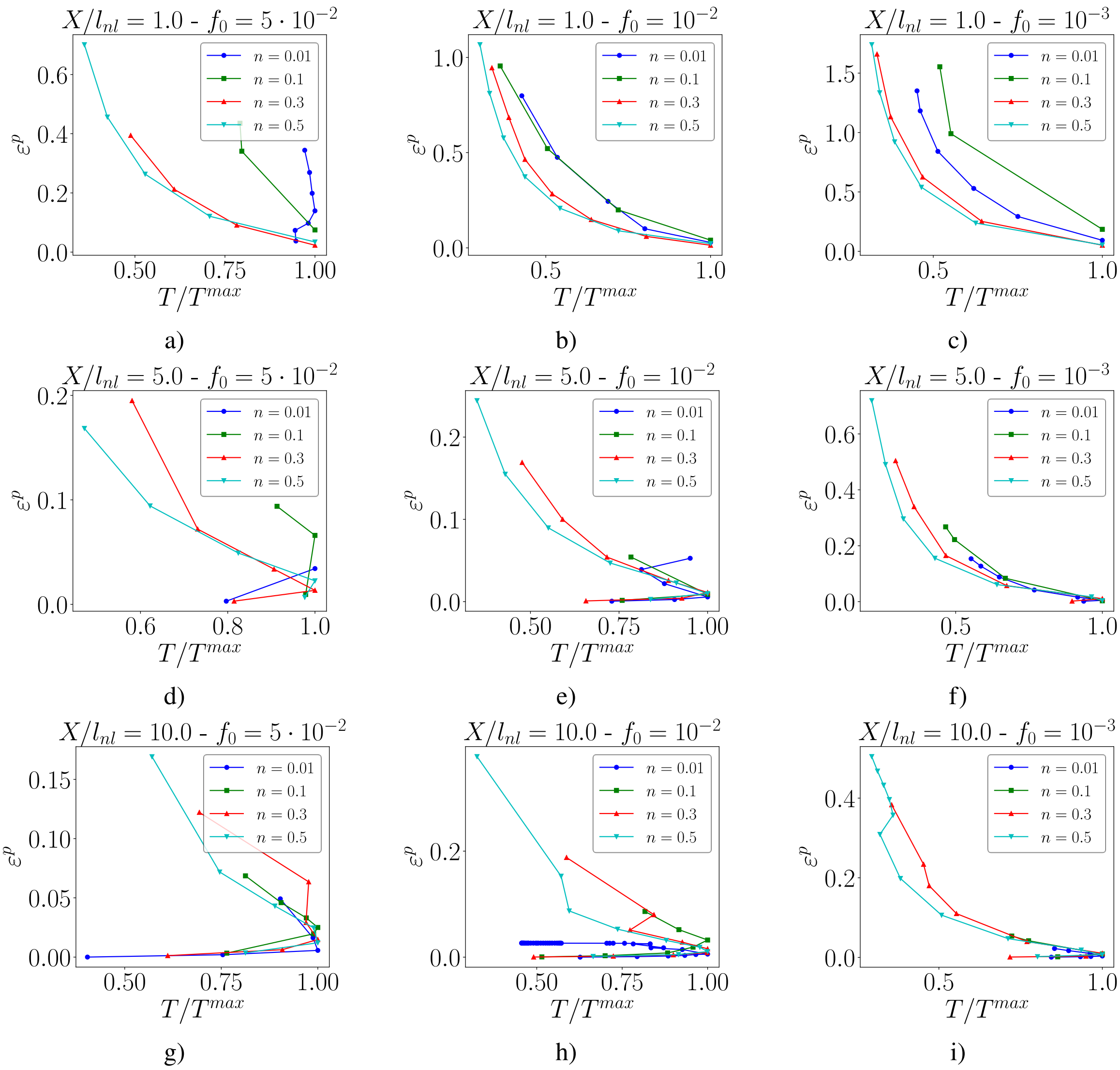

Figure B.30: Accumulated plastic strain evolution as a function of the stress triaxiality at three different distances X from the crack tip normalized by l_{nl}.

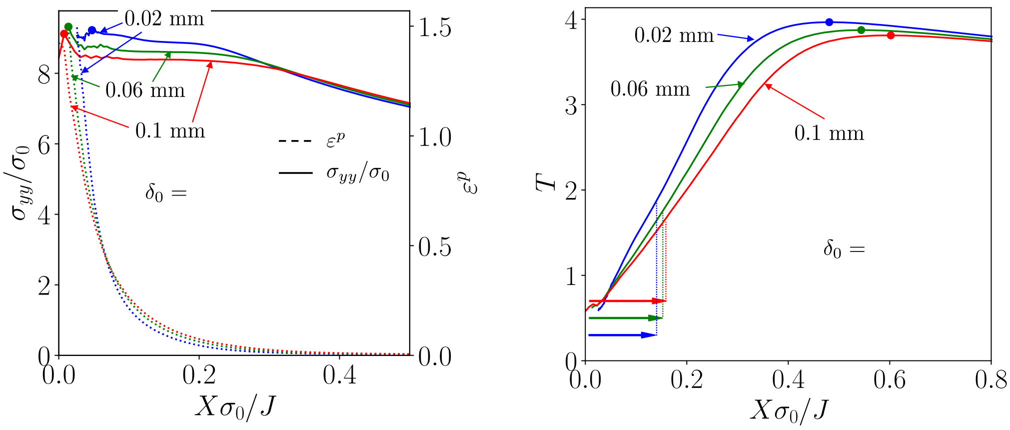

Figure C.31: Influence of the initial crack tip opening for a material with $n = 0.3$: a) Variation of the opening stress as a function of the normalized position; b) variation of the stress triaxiality and FPZ length as a function of the normalized position.

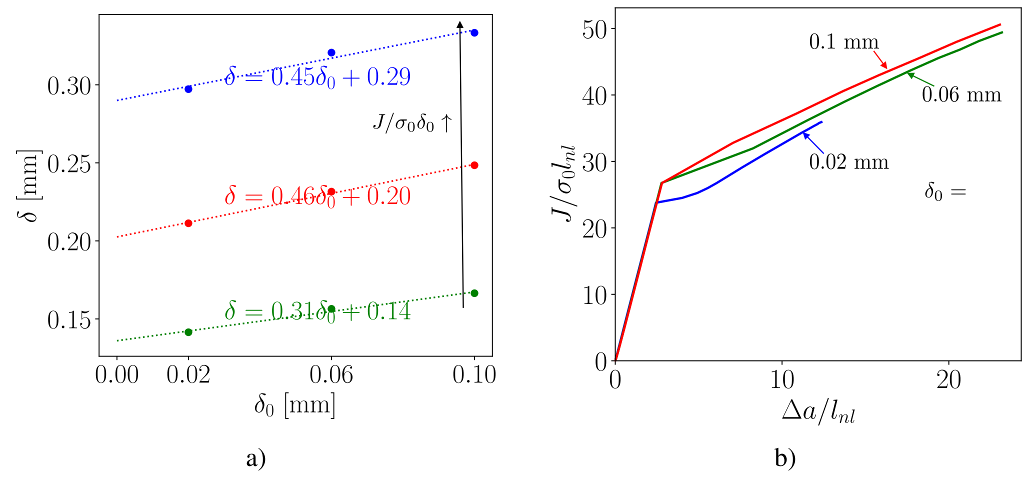

Figure C.32: a) Crack tip opening displacement as a function of the initial crack tip opening and of the applied loading; b) J_R curve as a function of the initial crack tip opening.

mesh convergence study. Fig. D.33 shows no discernible difference in the opening stress or accumulated plastic strain between the two codes, thereby confirming the behavior of materials characterized by $n = 0.5$.

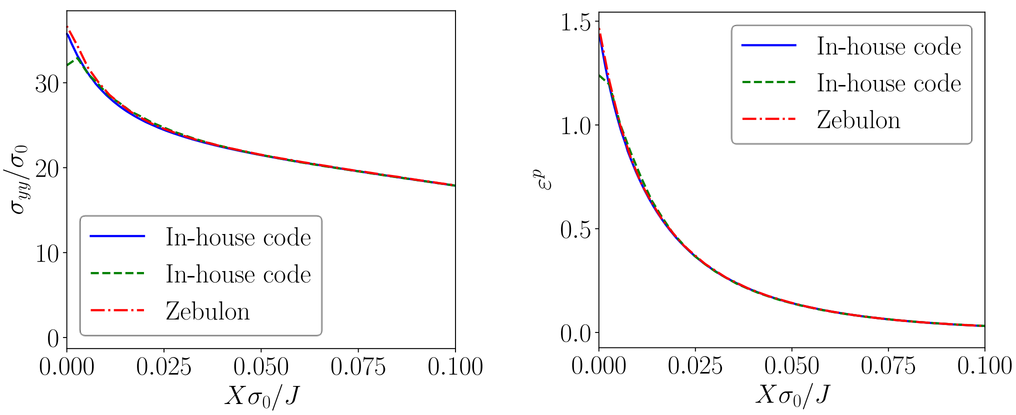

Figure D.33: Comparison between two FE codes: a) Variation of the opening stress as a function of the normalized position for $n = 0.5$ and $k = 666$; b) variation of the accumulated plastic strain as a function of the normalized position.

Appendix E. Rice and Tracey model

A fracture criterion based on the works of Rice and Tracey (1969) reads

$$\int_{R_0}^{R} \frac{dR}{R} = \int_0^{\varepsilon^p} 0.4\exp\left(\frac{3}{2}T\right) d\varepsilon^p \tag{E.1}$$

leading to

$$\ln \frac{R}{R_0} = D, \tag{E.2}$$

with D a damage indicator. As soon as D reaches a critical value D_c, fracture occurs. Fig. E.34a) depicts the stress triaxiality evolution as a function of the accumulated plastic strain. This curve will be used in Eq. (E.1) to compute D. Fig. E.34b) shows the damage evolution along the ligament. Also in this case, a lower value of n involves a lower D when looking at a given position $X\sigma_0/J$.

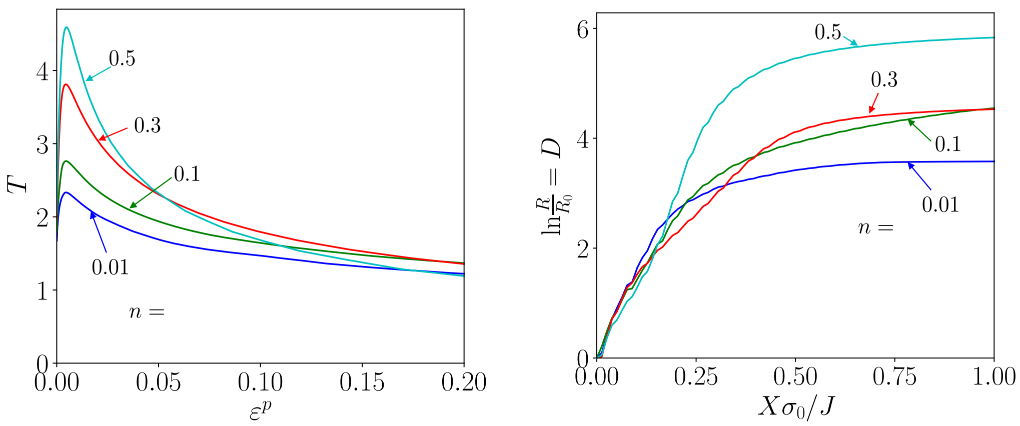

Figure E.34: Fracture criterion based on the Rice and Tracey model for different strain hardening exponent values and k = 666. a) Stress triaxiality evolution as a function of the accumulated plastic strain, b) damage evolution as a function of the normalized position.

References

Aravas, N., McMeeking, R., 1985. Finite element analysis of void growth near a blunting crack tip. Journal of the Mechanics and Physics of Solids 33, 25–49. URL: https://www.sciencedirect.com/science/article/pii/0022509685900201, doi:https://doi.org/10.1016/0022-5096(85)90020-1.

Benzerga, A.A., Leblond, J.B., 2010. Ductile fracture by void growth to coalescence, in: Aref, H., van der Giessen, E. (Eds.), Advances in Applied Mechanics. Elsevier. volume 44 of *Advances in Applied Mechanics*, pp. 169–305. URL: https://www.sciencedirect.com/science/article/pii/S006521561044003X, doi:https://doi.org/10.1016/S0065-2156(10)44003-X.

Benzerga, A.A., Leblond, J.B., Needleman, A., Tvergaard, V., 2016. Ductile failure modeling. International Journal of Fracture 201, 29–80. URL: http://dx.doi.org/10.1007/s10704-016-0142-6, doi:10.1007/s10704-016-0142-6.

Besson, J., Foerch, R., 1997. Large scale object-oriented finite element code design. Computer Methods in Applied Mechanics and Engineering 142, 165–187. URL: https://www.sciencedirect.com/science/article/pii/S0045782596011243, doi:https://doi.org/10.1016/S0045-7825(96)01124-3.

Bouby, C., Morin, L., Bignonnet, F., Dormieux, L., Kondo, D., 2023. On the thermodynamics consistency of gurson's model and its computational implications. International Journal of Solids and Structures 279, 112359. URL: http://dx.doi.org/10.1016/j.ijsolstr.2023.112359, doi:10.1016/j.ijsolstr.2023.112359.

Chen, Y., Lorentz, E., Besson, J., 2020. Crack initiation and propagation in small-scale yielding using a nonlocal gtn model. International Journal of Plasticity 130, 102701. URL: https://www.sciencedirect.com/science/article/pii/S0749641919304085, doi:https://doi.org/10.1016/j.ijplas.2020.102701.

Chu, C.C., Needleman, A., 1980. Void Nucleation Effects in Biaxially Stretched Sheets. Journal of Engineering Materials and Technology 102, 249–256. URL: https://doi.org/10.1115/1.3224807, doi:10.1115/1.3224807.

De Cooman, B.C., Estrin, Y., Kim, S.K., 2018. Twinning-induced plasticity (twip) steels. Acta Materialia 142, 283–362. URL: https://www.sciencedirect.com/science/article/pii/S1359645417305219, doi:https://doi.org/10.1016/j.actamat.2017.06.046.

Eleti, R.R., Klimova, M., Tikhonovsky, M., Stepanov, N., Zherebtsov, S., 2020. Exceptionally high strain-hardening and ductility due to transformation induced plasticity effect in ti-rich high-entropy alloys. Scientific Reports 10, 13293. URL: https://doi.org/10.1038/s41598-020-70298-2, doi:10.1038/s41598-020-70298-2.

Espeseth, V., Morin, D., Børvik, T., Hopperstad, O.S., 2023. A gradient-based non-local gtn model: Explicit finite element simulation of ductile damage and fracture. Engineering Fracture Mechanics 289, 109442. URL: https://www.sciencedirect.com/science/article/pii/S0013794423004009, doi:https://doi.org/10.1016/j.engfracmech.2023.109442.

Faleskog, J., Gao, X., Shih, C., 1998. Cell model for nonlinear fracture analysis - i. micromechanics calibration. International Journal of Fracture 89, 355–373. doi:10.1023/A:1007421420901.

Gologanu, M., Leblond, J.B., Devaux, J., 1993. Approximate models for ductile metals containing non-spherical voids—case of axisymmetric prolate ellipsoidal cavities. Journal of the Mechanics and Physics of Solids 41, 1723–1754. URL: https://www.sciencedirect.com/science/article/pii/002250969390029F, doi:https://doi.org/10.1016/0022-5096(93)90029-F.

Grässel, O., Krüger, L., Frommeyer, G., Meyer, L., 2000. High strength fe–mn–(al, si) trip/twip steels development — properties — application. International Journal of Plasticity 16, 1391–1409. URL: https://www.sciencedirect.com/science/article/pii/S0749641900000152, doi:https://doi.org/10.1016/S0749-6419(00)00015-2.

Gullerud, A., Dodds, R., Hampton, R., Dawicke, D., 1999. Three-dimensional modeling of ductile crack growth in thin sheet metals: computational aspects and validation. Engineering Fracture Mechanics 63, 347–374. URL: https://www.sciencedirect.com/science/article/pii/S001379449900034X, doi:https://doi.org/10.1016/S0013-7944(99)00034-X.

Hilhorst, A., Jacques, P.J., Pardoen, T., 2023. Towards the best strength, ductility, and toughness combination: High entropy alloys are excellent, stainless steels are exceptional. Acta Materialia 260, 119280. URL: https://www.sciencedirect.com/science/article/pii/S1359645423006109, doi:https://doi.org/10.1016/j.actamat.2023.119280.

Hilhorst, A., Leclerc, J., Pardoen, T., Jacques, P.J., Noels, L., Nguyen, V.D., 2022. Ductile fracture of high entropy alloys: From the design of an experimental campaign to the development of a micromechanics-based modeling framework. Engineering Fracture Mechanics 275, 108844. URL: https://www.sciencedirect.com/science/article/pii/S0013794422005628, doi:https://doi.org/10.1016/j.engfracmech.2022.108844.

Hutchinson, J., 1968. Plastic stress and strain fields at a crack tip. Journal of the Mechanics and Physics of Solids 16, 337–342. URL: https://www.sciencedirect.com/science/article/pii/0022509668900215, doi:https://doi.org/10.1016/0022-5096(68)90021-5.

Hutchinson, J., 1974. On steady quasi-static crack growth. Harvard University Report DEAP S-8 .

Hutchinson, J., Tvergaard, V., 1989. Softening Due to Void Nucleation in Metals, in: Fracture Mechanics: Perspectives and Directions (Twentieth Symposium). ASTM International. URL: https://doi.org/10.1520/STP18820S, doi:10.1520/STP18820S.

Leblond, J.B., Perrin, G., Devaux, J., 1995. An improved gurson-type model for hardenable ductile metals. European Journal of Mechanics A-solids 14, 499–527. URL: https://api.semanticscholar.org/CorpusID:118050919.

Lecarme, L., Tekoğlu, C., Pardoen, T., 2011. Void growth and coalescence in ductile solids with stage iii and stage iv strain hardening. International Journal of Plasticity 27, 1203–1223. doi:10.1016/j.ijplas.2011.01.004.

McMeeking, R., 1977. Finite deformation analysis of crack-tip opening in elastic-plastic materials and implications for fracture. Journal of the Mechanics and Physics of Solids 25, 357–381. URL: https://www.sciencedirect.com/science/article/pii/0022509677900035, doi:https://doi.org/10.1016/0022-5096(77)90003-5.

Narasimhan, R., Rosakis, A., 1988. A finite element analysis of small-scale yielding near a stationary crack under plane stress. Journal of the Mechanics and Physics of Solids 36, 77–117. URL: https://www.sciencedirect.com/science/article/pii/002250968890021X, doi:https://doi.org/10.1016/0022-5096(88)90021-X.

Needleman, A., Tvergaard, V., 1984. An analysis of ductile rupture in notched bars. Journal of the Mechanics and Physics of Solids 32, 461–490. URL: https://www.sciencedirect.com/science/article/pii/0022509684900310, doi:https://doi.org/10.1016/0022-5096(84)90031-0.

Nguyen, V.D., Pardoen, T., Noels, L., 2020. A nonlocal approach of ductile failure incorporating void growth, internal necking, and shear dominated coalescence mechanisms. Journal of the Mechanics and Physics of Solids 137, 103891. URL: https://www.sciencedirect.com/science/article/pii/S0022509619309275, doi:https://doi.org/10.1016/j.jmps.2020.103891.

Nielsen, K., Pardoen, T., Tvergaard, V., de Meester, B., Simar, A., 2010. Modelling of plastic flow localisation and damage development in friction stir welded 6005a aluminium alloy using physics based strain hardening law. International Journal of Solids and Structures 47, 2359–2370. URL: http://dx.doi.org/10.1016/j.ijsolstr.2010.03.019, doi:10.1016/j.ijsolstr.2010.03.019.

O'Dowd, N.P., Shih, C., Dodds, R.H., 1995. The role of geometry and crack growth on constraint and implications for ductile/brittle fracture, in: Constraint Effects in Fracture Theory and Applicatons: Second Volume. ASTM International.

Pardoen, T., Hachez, F., Marchioni, B., Blyth, P., Atkins, A., 2004. Mode i fracture of sheet metal. Journal of the Mechanics and Physics of Solids 52, 423–452. URL: https://www.sciencedirect.com/science/article/pii/S0022509603000875, doi:https://doi.org/10.1016/S0022-5096(03)00087-5.

Pardoen, T., Hutchinson, J., 2000. An extended model for void growth and coalescence. Journal of the Mechanics and Physics of Solids 48, 2467–2512. URL: https://www.sciencedirect.com/science/article/pii/S0022509600000193, doi:https://doi.org/10.1016/S0022-5096(00)00019-3.

Pardoen, T., Hutchinson, J., 2003. Micromechanics-based model for trends in toughness of ductile metals. Acta Materialia 51, 133–148. URL: https://www.sciencedirect.com/science/article/pii/S1359645402003865, doi:https://doi.org/10.1016/S1359-6454(02)00386-5.

Peerlings, R., Borst, de, R., Brekelmans, W., Geers, M., 1998. Gradient-enhanced damage modelling of concrete fracture. Mechanics of Cohesive-Frictional Materials 3, 323–342. doi:10.1002/(SICI)1099-1484(1998100)3:4<323::AID-CFM51>3.0.CO;2-Z.

Rice, J., Rosengren, G., 1968. Plane strain deformation near a crack tip in a power-law hardening material. Journal of the Mechanics and Physics of Solids 16, 1–12. URL: https://www.sciencedirect.com/science/article/pii/0022509668900136, doi:https://doi.org/10.1016/0022-5096(68)90013-6.

Rice, J., Sorensen, E., 1978. Continuing crack-tip deformation and fracture for plane-strain crack growth in elastic-plastic solids. Journal of the Mechanics and Physics of Solids 26, 163–186. URL: https://www.sciencedirect.com/science/article/pii/0022509678900078, doi:https://doi.org/10.1016/0022-5096(78)90007-8.

Rice, J., Tracey, D., 1969. On the ductile enlargement of voids in triaxial stress fields. Journal of the Mechanics and Physics of Solids 17, 201–217. URL: https://www.sciencedirect.com/science/article/pii/0022509669900337, doi:https://doi.org/10.1016/0022-5096(69)90033-7.

Rice, J.R., Johnson, M.A., 1969. The Role of Large Crack Tip Geometry Changes in Plane Strain Fracture. Technical report (Brown University. Division of Engineering), Division of Engineering, Brown University. URL: https://books.google.be/books?id=hCRnHQAACAAJ.

Roubaud, F., Morin, L., Remmal, A., Marie, S., Leblond, J.B., 2024. A gurson-type layer model for ductile porous solids containing ellipsoidal voids with isotropic and kinematic hardening. European Journal of Mechanics - A/Solids 104, 105114. URL: http://dx.doi.org/10.1016/j.euromechsol.2023.105114, doi:10.1016/j.euromechsol.2023.105114.

Schaal, H., Castany, P., Gloriant, T., 2023. Outstanding strain-hardening of a new metastable β-titanium alloy elaborated by in situ additive manufacturing l-pbf process. Materials Science and Engineering: A 875, 145117. URL: https://www.sciencedirect.com/science/article/pii/S0921509323005415, doi:https://doi.org/10.1016/j.msea.2023.145117.

Scheyvaerts, F., Onck, P., Tekoğlu, C., Pardoen, T., 2011. The growth and coalescence of ellipsoidal voids in plane strain under combined shear and tension. Journal of the Mechanics and Physics of Solids 59, 373–397. URL: http://dx.doi.org/10.1016/j.jmps.2010.10.003, doi:10.1016/j.jmps.2010.10.003.

Tvergaard, V., 1981. Influence of voids on shear band instabilities under plane strain conditions. International Journal of Fracture 17, 389–407. URL: http://dx.doi.org/10.1007/BF00036191, doi:10.1007/bf00036191.

Tvergaard, V., Hutchinson, J.W., 1992. The relation between crack growth resistance and fracture process parameters in elastic-plastic solids. Journal of the Mechanics and Physics of Solids 40, 1377–1397. URL: https://www.sciencedirect.com/science/article/pii/0022509692900203, doi:https://doi.org/10.1016/0022-5096(92)90020-3.

Tvergaard, V., Needleman, A., 1984. Analysis of the cup-cone fracture in a round tensile bar. Acta Metallurgica 32, 157–169. URL: https://www.sciencedirect.com/science/article/pii/000161608490213X, doi:https://doi.org/10.1016/0001-6160(84)90213-X.

Xia, L., Shih, C., 1995. Ductile crack growth-i. a numerical study using computational cells with microstructurally-based length scales. Journal of the Mechanics and Physics of Solids 43, 233–259. URL: https://www.sciencedirect.com/science/article/pii/002250969400064C, doi:https://doi.org/10.1016/0022-5096(94)00064-C.

Xia, L., Shih, C., Hutchinson, J.W., 1995. A computational approach to ductile crack growth under large scale yielding conditions. Journal of the Mechanics and Physics of Solids 43, 389–413. URL: https://www.sciencedirect.com/science/article/pii/002250969400069H, doi:https://doi.org/10.1016/0022-5096(94)00069-H.

Yoshida, K., Kuwabara, T., 2007. Effect of strain hardening behavior on forming limit stresses of steel tube subjected to nonproportional loading paths. International Journal of Plasticity 23, 1260–1284. URL: https://www.sciencedirect.com/science/article/pii/S0749641906001604, doi:https://doi.org/10.1016/j.ijplas.2006.11.008.

Zhang, Y., Lorentz, E., Besson, J., 2018. Ductile damage modelling with locking-free regularised gtn model. International Journal for Numerical Methods in Engineering 113, 1871–1903. URL: https://onlinelibrary.wiley.com/doi/abs/10.1002/nme.5722, doi:https://doi.org/10.1002/nme.5722, arXiv:https://onlinelibrary.wiley.com/doi/pdf/10.1002/nme.5722.